Research Paper

Statistical volume element averaging scheme for fracture of quasi-brittle materials

Justin M. Garrard, Reza Abedi*

Department of Mechanical, Aerospace and Biomedical Engineering, The University of Tennessee at Knoxville/Space Institute, TN, USA

ARTICLE INFO

ABSTRACT

To capture the randomness and inhomogeneity of rock at microscale, a statistical volume element (SVE) averaging approach is proposed. The microcrack statistics of a real-world Yuen-Long marble sample is used to realize 2D microcracked domains. The size effect, *i.e.* the decrease of the mean and variation of homogenized strength field by increasing SVE size, is analyzed. Increasing the crack density is shown to have a similar effect. While smaller SVEs maintain a greater level of inhomogeneity and are preferred for fracture analysis, it is shown that low density of microcracks pose a lower limit on the SVE size. Beside the actual power-law distribution of microcrack length, by varying the Weibull model shape parameter m other domains are created with different microcrack distribution shapes. Macroscopic fracture simulations, by the asynchronous Spacetime Discontinuous Galerkin (aSDG) method, study the effect of m for a uniaxial tensile problem. By increasing m from 0.5 to 4, the length distribution of microcracks become more uniform; this corresponds to a more uniform and stronger mesoscopic strength field, which results to about 3 and 6 times increase to macroscopic tensile strength and toughness, respectively. However, the more uniform length distribution of microcracks is shown to reduce rock brittleness.

1. Introduction

Understanding the behavior of rock, including how it is materially constituted, reacts to loading, and fails is vital for critical economic activities such as mining, drilling, tunneling, and construction. While these activities may consider the material in the macro-scale, the behavior of quasi-brittle materials such as rock is heavily influenced by heterogeneity at the meso- and micro-scale [1–3]. Because brittle materials lack energy dissipative mechanisms, microcrack stress concentrations are not balanced as in more ductile materials and directly influence the material's peek and post-instability response [4]. The distribution of microcracks and voids change the overall response of the system to an applied stress. These heterogeneities result in crack pattern variability between multiple samples for similar loading [5] and uncertainty in the ultimate fracture strength of the material [6,4]. The *size effect*, where the sample-to-sample mean and variation of fracture strength of a given material decreases with increasing structure size [7,3], is a well-known phenomenon for quasi-brittle materials. The size effect for these materials is contributed to the distribution of microscale defects and insignificance of plasticity or other mechanisms that could otherwise absorb large energies and significantly redistribute the stress field [2].

Simulating the effect of these heterogeneities can be performed either explicitly or implicitly [8]. *Explicit* models directly incorporate defects greater than some minimum size into the analysis. For example, as in [9–12] the continuum is simplified as a network of bars or beams with random properties. *Peridynamic* [13], *discrete element methods* [14,15], and *discrete particle methods* [16] are other examples that can model continuum as a collection of (possibly deformable) particles. Another example is the explicit representation of (micro) cracks in a computational framework. The explicit representation of defects in general improves the fidelity of computational model. For example, explicit representation of microcracks is important in hydraulic fracturing applications [17]. Moreover, explicit models can even be used to explain highly complex phenomena such as solid- to fluid-like transition in sand dunes [18].

Implementing explicit models is computationally costly; so there is great difficulty in employing these models for anything other than small space and time scales. *Implicit* models represent the microstructure in an averaged or homogenized sense, and have been used to qualitatively explain the size effect. The implicit representation of microstructures makes implicit methods computationally more affordable than explicit ones. A popular implicit model is Weibull's weakest link model [19,20]. This model has been used to show that realistic fracture patterns can be

---

captured for problems that lack macroscopic stress concentration points, such as fragmentation [21] and dynamic compressive loading [22] problems. The main issue with these models is that while they are able to capture the general phenomenon, they lack a direct physical connection to the material microstructure. Therefore, an approach is necessary that can link the microstructural distribution of defects to the macro-scale, without the computational costs required of explicit models.

Homogenization methods address this concern by averaging the effect of the microstructure in a *volume element* (VE). In continuum mechanics, a *Representative Volume Element* (RVE) acts as a mathematical point of a continuum field approximating the true material microstructure. The equivalent term *Representative Elementary Volume* (REV) is used in rock mechanics. According to [23], RVEs are well-defined for a unit cell in a periodic microstructure and a statistically representative volume containing very large number of microscale elements. In this manuscript, our focus is on the second type of VEs. For a macroscopically homogeneous material with ergodic properties the standard deviation of the homogenized properties follows a power law [24] or model [25,26] versus the VE size, in that, the variation of homogenized properties tend to zero as the VE size tends to infinity. The RVE size for a given material property of a composite is chosen such that either this standard deviation, or the error in estimating the mean of the homogenized property, falls below a user-specified tolerance for a given number of VE realizations; *cf.* [27,26,28,29] on more detailed discussion on the RVE and the determination of its size.

For a given material property, if the aforementioned condition for the RVE size is not satisfied, the VEs are known as *Statistical Volume Elements* (SVEs). These SVEs are smaller than the corresponding RVE, and simply speaking a large variation is observed in properties homogenized by SVEs. One advantage of SVEs is that they can model spatial and sample-to-sample variation of material properties by using small enough VEs for homogenization. The selected SVE observation window [30,31], type of boundary conditions [32], and clustering of microstructures [33] all affect the statistics of the homogenized properties.

While RVEs have been used in many studies to homogenize and calibrate various fracture models [34–38], the use of SVEs provides several advantages for fracture analysis; by maintaining material inhomogeneity in fracture properties, fracture can initiate from material weak points, as opposed to unrealistic fracture initiation from all points under a spatially uniform stress field as shown in [39]. Moreover, by preserving sample-to-sample variations, variations in fracture pattern, ultimate load, and fracture strengths for different samples can be captured when SVEs are used. Finally, it is noted that by homogenizing the effect of microstructure into heterogeneous material property fields, the use of SVEs provides a significant advantage in computational cost over explicit methods.

We have previously used SVEs for fracture analysis of quasi-brittle materials with microcracks in [39–41]. However, the microcrack statistics were not derived from any known material and instead were simply used to detail the overall analysis process. In addition, no crack interaction was considered. We address these shortcomings in this manuscript; first, a data set [42,43] which contained the microcrack distribution statistics for a set of six Yuen-Long marble samples was identified for this analysis. As in the paper by Wong et al., a power law distribution was used to match the microcrack length distribution in the simulated Yuen-Long marble RVE domain. Second, a sliding wing crack model was used [44] to take into account the effect of crack interaction caused by crack fields with differing densities and crack distributions. These efforts improve the accuracy of microcrack statistics and the homogenized mesoscopic fracture strength fields.

The distribution of microcrack length can have a significant effect on both homogenized mesoscopic strength fields and macroscopic fracture response. To better analyze such effect, we create synthetic rock samples where crack length follows a Weibull distribution, while the mean of crack length matches that of the original Yuen-Long marble

sample data. The Weibull model is used to create very different crack length distributions by simply changing the Weibull shape parameter. Finally, we study the effect of crack density and SVE size on the statistics of homogenized fracture strength fields.

Relating the statistics of microcracks to macroscopic fracture response is the second contribution of this manuscript, which is done by simulating domains with SVE-homogenized fracture strength fields. These fields are simulated using an *asynchronous Spacetime Discontinuous Galerkin method* (aSDG) [45,46]. The proposed multiscale approach based on the use of SVEs greatly reduces computational cost relative to the direct numerical simulation of rock. At the macroscale, we derive macroscopic strain versus stress responses for a uniaxial tensile problem. The macroscopic simulations are used to demonstrate the effect of initial crack distribution on macroscopic rock strength, toughness, brittleness, and fracture pattern. One general observation is that domains with more uniform crack length distribution can sustain a larger macroscopic stress level, but have a more brittle response.

The remainder of manuscript is structured as follows. In Section 2 the SVE analysis process is described as well as the relevant background material from [43]. Results for the Yuen-Long material crack distribution and differing Weibull crack length model distributions are provided in Section 3. In this section, microcrack statistics are translated to an inhomogeneous mesoscopic fracture strength field, which is subsequently used in Section 4 for dynamic macroscopic fracture analysis. Final discussion of the results and future work are discussed in Section 5.

2. Materials and methods

Fig. 1 depicts an outline for this section. In [43], the authors consider a 32 mm by 32 mm square domain of Yuen-Long marble to be representative. That is, the size of domain is large enough to contain sufficient number of microcracks and is sufficiently larger than the size of microcracks measured in their experiments. This ensures that properties homogenized on this size demonstrate very small variations from sample to sample. Herein, we refer to a square domain of this size as a *Representative Volume Element* (RVE). In Section 2.1 we describe the process in which we populate microcrack with specific length and angle distributions in the macroscopic domain.

Instead of directly deriving material properties such as fracture strength for RVEs, we are interested in assigning such properties for *Statistical Volume Elements* (SVEs). The use of SVEs ensures that derived properties are no longer uniform for a macroscopically homogeneous rock. Moreover, each SVE maintains sample-to-sample variation for a given property at the same spatial location between different RVEs. As shown in Fig. 1(a), we use circular SVEs of size L_{SVE} to traverse the RVE with spacing S. Fig. 1(b) shows a zoomed view of an SVE containing multiple microcracks. The formation of SVEs within the RVE and the characterization of a unique mesoscopic compressive fracture strength per SVE are described in Sections 2.2 and 2.3, respectively. Once the RVE is traversed with SVEs, at the center of each SVE a unique mesoscopic strength value is assigned. A contour plot generated from grid values of these strengths is shown in Fig. 1(c). Finally, any of such inhomogeneous mesoscopic fields can be used as an input fracture strength field for a macroscopic fracture simulation of an RVE. Fig. 1(d) shows a sample fracture pattern obtained by the aSDG method.

2.1. Distribution of microcracks

While the actual microcrack distribution of the material microstructure for each Yuen-Long marble sample is not given in [43], the provided material properties and microcrack statistics allows us to generate random realizations of the material that accurately represent the material behavior. These realizations contain a field of microcracks with realistic crack length distributions, crack angle distributions, and the correct microcrack density in the domain. The microcrack statistics
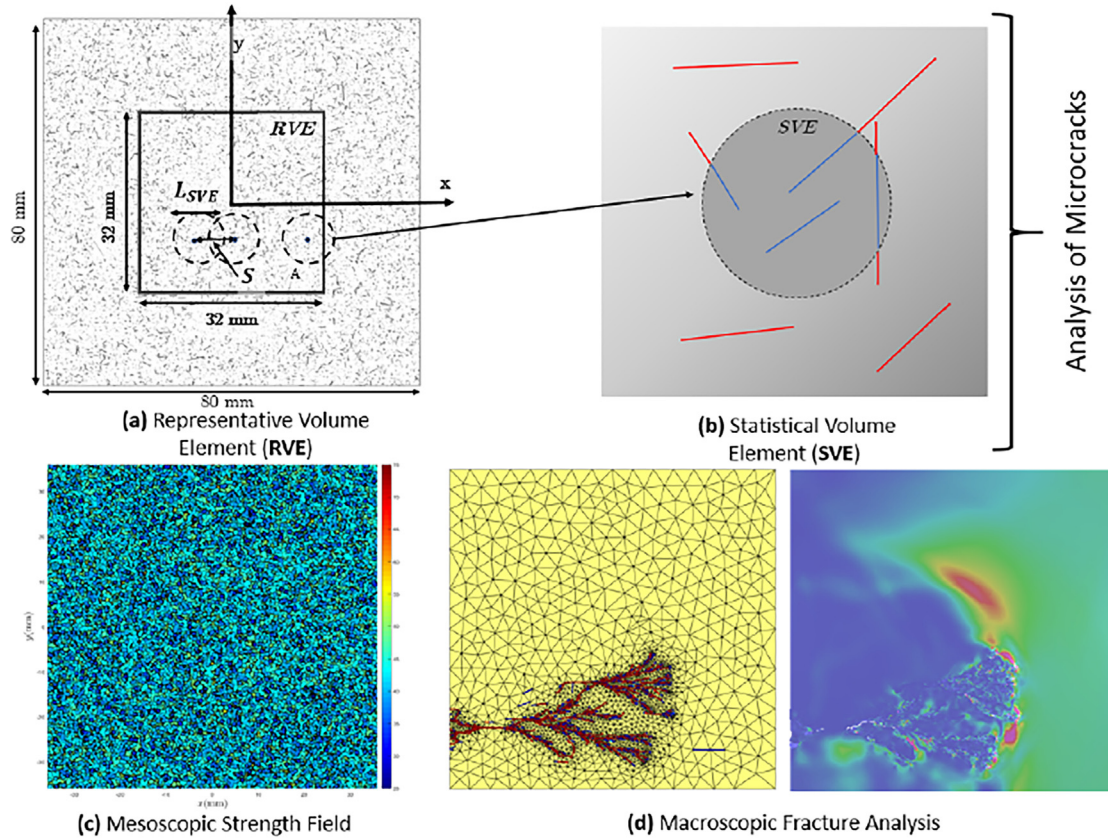
Fig. 1. A multi-scale model for fracture analysis of microcracked rock.

and material Poisson's ratio and modulus of elasticity were taken from the material sample designated S19 in [43]. The spatial distribution of the individual cracks remains random for each realization. Therefore, this section will describe the statistical distributions used to create the randomly generated domains. While the information contained herein is not original, this section acts as a review of the information required to generate the random domains.

We first discuss the distribution of the length of microcracks. Crack length is indirectly specified by its half length a, as is common in the field of fracture mechanics. From [43] for the given marble, a is shown to follow a power law distribution. Because a power law distribution will blow up with decreasing crack size, a minimum half crack length a' is assigned. Therefore, the cumulative probability for half cracks longer than a' for an elemental volume V_0 is defined as,

$$g(a) = \left(\frac{q^*}{a}\right)^z \tag{1}$$

where q^* and Cauchy distribution exponent $z > 1$ are the parameters of the power distribution, subject to the condition,

$$V_0 \int_{a'}^{\infty} g(a)da = 1. \tag{2}$$

To ensure this equality, the lower integration limit, a' is defined by,

$$a' = \left[\frac{(q^*)^z V_0}{z-1}\right]^{\frac{1}{z-1}} \tag{3}$$

This half crack length distribution was used to create new random crack field realizations with the provided marble properties that are given in [43] and described in Section 3. The angular distribution of the cracks was assumed to follow a uniform distribution, corresponding to a macroscopically isotropic material. The spatial location of cracks is also assumed to follow a uniform distribution, corresponding to a macroscopically homogeneous material. The last descriptor used for realizing

microcracked domains is crack density ε_0, defined as the nondimensional sum of the squares of individual crack lengths per unit surface area. To generate a statistically consistent domain such as that shown in Fig. 1(a), individual cracks are created and placed in the domain by a pick-and-place algorithm in which for an individual crack its half length, angle, and spatial location are sampled from their corresponding distribution functions. Individual cracks are placed in the domain until the target crack density is reached.

To investigate how the distribution of half crack length affects fracture response, several additional domains were created with similar material properties as the Yuen-Long marble samples and maintaining the same mean half crack length as that of the power law distribution in [43]. However, rather than using a power law distribution, a Weibull distribution was used due to the ease in changing the shape of the distribution utilizing the shape parameter m. The Weibull cumulative distribution function for a is defined as,

$$g(a) = 1 - e^{-r\left[\frac{a-\gamma}{\eta}\right]^m} \tag{4}$$

As stated previously, the power m is the shape parameter, which controls the shape of the distribution. The Weibull model parameters are calibrated for an elemental volume V_0. The distribution for another elemental volume V is adjusted through the ratio $r := V/V_0$. Moreover, η is the scale parameter and γ, similar to a', controls the minimum half crack length of the distribution. To change the shape of the distribution, several different m values were selected for analysis. To maintain the minimum half crack length, the γ value was set equal to a'. Therefore, the only variable which was changed between the given distributions to retain the mean crack length was η.

2.2. SVE characterization
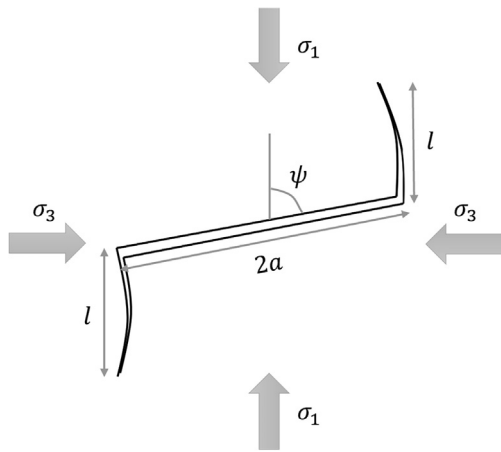
The most important aspect affecting material properties

J.M. Garrard and R. Abedi

Computers and Geotechnics 117 (2020) 103229

Fig. 2. Sliding wing crack model with orientation of wings relative to principal compressive stresses σ_1 and σ_3.

Fig. 3. SVE containing cracks for fracture analysis (Red lines are considered crack segments external to SVE, Blue lines are considered crack segments internal to SVE). (For interpretation of the references to color in this figure legend, the reader is referred to the web version of this article.)

Table 1
Sample S19 material properties taken from [43].

ρ (kg/m³)	ν	E (GPa)	$2a$ (mm)	a' (mm)	ε_0	z	q^*V_0
2727	0.25	34.65	0.141	0.0075	0.243	2.017	0.007

homogenized or averaged by SVEs is the size of SVE, L_{SVE}. As L_{SVE} increases toward the RVE size and beyond, the material properties become more uniform; for a macroscopically homogeneous material the values obtained from all SVEs in fact tend to a unique value. The size of SVEs should be chosen considerably smaller than RVE size limit. On the other hand, the SVE size must be sufficiently larger than the microstructural details of the material and ideally contain a sufficient number of them in the SVE to make it representative of the response of the material. For the problem considered herein, microstructure is characterized by microcracks whose length distribution was described in Section 2.1. To ensure SVEs are larger than the typical microstructure size, we require the relative size of SVE by mean crack length, defined by $\beta = L_{SVE}/\mathbb{E}(2a)$, be larger than one. Moreover, to ensure that SVEs are representative, ideally we want to have majority of SVEs to contain some microcracks. For the SVEs which do not contain any cracks, a maximum fracture strength corresponding to minimum allowable crack length of the distributions discussed in Section 2.1 is assigned. As will be shown in Section 3.4, the condition of SVEs containing microcracks further constrains the lower limit of L_{SVE} at low crack densities. In addition, it is shown that the mean and standard deviation of fracture strength decrease as L_{SVE} increases.

The second consideration is the shape of an SVE. In 2D, square and rectangle are typical shapes for SVEs. However, herein we consider circular SVEs for two reasons. First, in [47] it is shown that the square SVEs artificially make the homogenized material anisotropic (even if it is isotropic at macroscale), in that homogenized properties have a nonphysical bias (minimum or maximum value) along 0/90 or 45/135 degrees. While unlike [40,41], we do not consider angular dependency of the fracture strength, the circular shape still eliminates artificially higher or lower strengths along these angles to be incorporated in the fracture strength of SVEs. Second, the circular shape of an SVE simplifies the algorithm to determine the intersection of a crack with an SVE, as it is needed to determine its strength in Section 2.3.

We use circular SVEs in the context of *moving window* [31,48,49] method, wherein overlapping *windows* (volume elements) smaller than RVE scale traverse the domain in the context of *Generalized Method of Cells* (GMC). The square SVEs in [48,49] and circular ones in present study are overlapping and are centered at the points of a fine structured grid. As shown in Fig. 1(a), the spacing of SVEs, *i.e.* the center to center distance of consecutive SVEs in horizontal and vertical directions, is denoted by S. For any given SVE size, we use the spacing $S = L_{SVE}/n$, for a spacing factor n equal or greater than 5. In Section 3.1.1, we perform a review of several SVE spacing values in order to determine a reasonable value for n. After this review, it was determined that by using the spacing $n = 10$, the characterized inhomogeneous fracture strength field will be of high spatial resolution while retaining computational
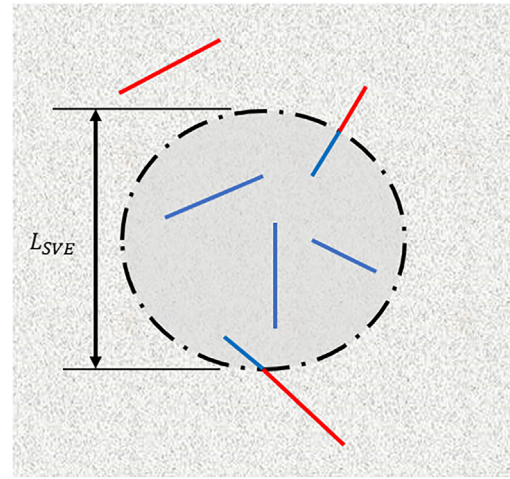
efficiency; *cf.* Fig. 1(c). For the 32 mm by 32 mm RVE in Fig. 1(a), this corresponds to a $32/S + 1$ by $32/S + 1$ square grid; at each grid point the averaged fracture strength, *cf.* Section 2.3, of an SVE centered at that point is assigned. To ensure the SVEs close to the boundary of the RVE (for example SVE A in Fig. 1(a)) entirely cover the microcracked rock, we need to choose a volume element larger than the RVE size. In this study, a 80 mm by 80 mm volume element is chosen for this volume element.

2.3. Mesoscopic fracture strength model

We note that in the present study only fracture strength is considered as an inhomogeneous/ random field at the mesoscale, and elastic properties are deemed to be homogeneous. This is consistent with the approach in [42,43]. In addition, fracture strength has been the field that is considered inhomogeneous in majority of similar studies, see for example [50–55].

Assigning a fracture strength to an SVE involves two steps. The first step is the determination of uniaxial compressive fracture strength s_c for a single crack contained in a domain with a specific crack density. To ensure consistent strength values with the data set produced by Wong et al., [42,43], the same sliding wing crack strength model for uniaxial compressive strength is utilized in this manuscript. This section summarizes the fracture strength model given in [43] used to calculate the fracture strengths in this manuscript.

The wing crack model relates the compressive failure stress to the critical stress intensity factor, K_{IC}. It considers the tensile stress concentration at the tips of the inclined preexisting cracks of length $2a$. The applied stresses induce a shear traction on the plane of the crack, which if sufficiently high to overcome the frictional resistance along the closed crack, results in stress concentrations that may induce wing cracks to propagate, as shown in Fig. 2. This propagation is characterized by the stress intensity factor K_I at the point of wing crack initiation which is a function of the friction coefficient μ, the angle ψ between the crack and maximum compressive principal stress σ_1, and the applied stress field. While the fracture strength equations for the wing-crack model can be

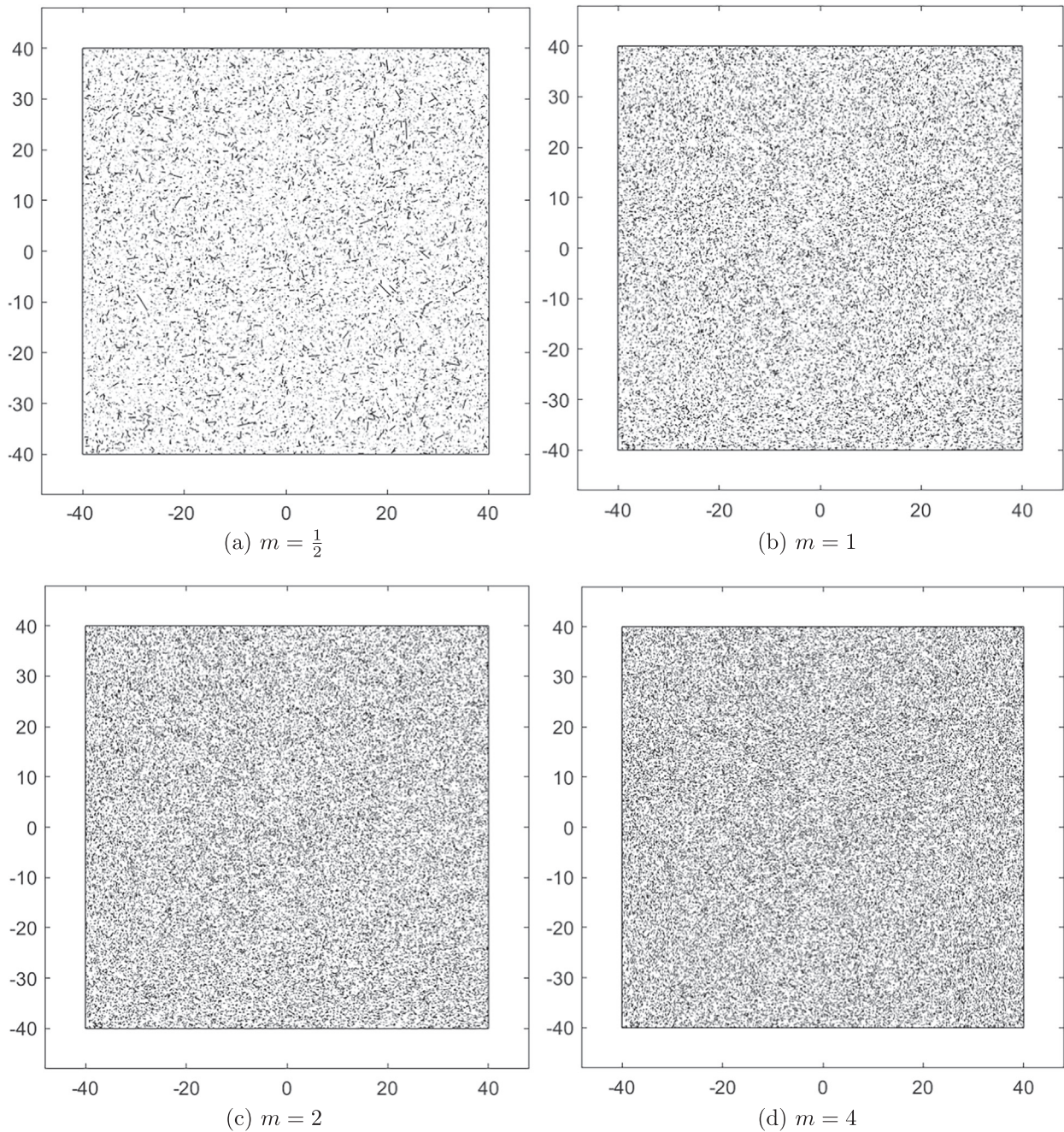(a) $m = \frac{1}{2}$ (b) $m = 1$ (c) $m = 2$ (d) $m = 4$

Fig. 4. Representative generated microcrack domains for various m Weibull crack length distributions for $\varepsilon_0 = 0.243$.

found in [43], we have reproduced the equations (Eqs. (5)–(7)) here for clarity.

When the loading is increased, the stress intensity factor K_I approaches the critical value K_{IC} at which point the wing crack grows out of the initial plane along orientations sub-parallel to σ_I. As the stress increases, more cracks distributed throughout the given sample will grow in this form. These cracks will eventually coalesce. One benefit of the wing crack model in [43] is that this complex crack interaction is captured by analytic approximations in the model. So, the given compressive strength is given by,

$$s_c = \frac{K_{IC}}{y\sqrt{\pi a}},$$

(5)

where y denotes crack interaction in an averaged sense. In [44] the value of y is derived for a structured grid of parallel wing cracks and was used in [43] to approximately model their interaction for a non-structured network of wing cracks (variable size, angle, and spacing). The value of y is obtained from,

$$y = \frac{\sqrt{1+\mu^2} - \mu}{(1+l_{cr})^{3/2}} \left[C_3 l_{cr} + \frac{1}{\sqrt{3}(1+l_{cr})^{1/2}} \right] + \frac{[2\varepsilon_0(l_{cr} + \cos\psi)]^{1/2}}{\sqrt{\pi}}.$$

(6)

In (6), μ is the friction coefficient, ψ is the angle between the sliding crack and the maximum principal stress, l_{cr} is the critical normalized crack length, and ε_0 is the crack density. C_3 will be defined as part of the solution for the normalized critical length l_{cr}, which is a positive root of the implicit equation,
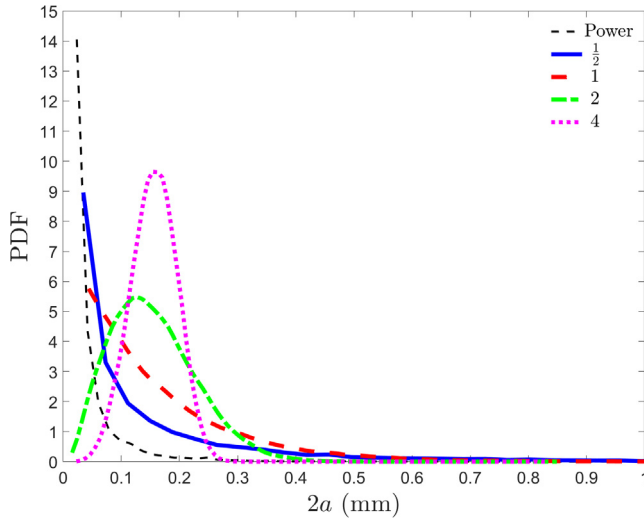
Fig. 5. Probability density function of crack length $2a$ for generated power distribution and Weibull domains with $\varepsilon_0 = 0.243$.

$$\frac{C_1}{2(l + \cos\psi)^{1/2}} + \frac{C_2}{(1 + l)^{3/2}}\left[C_3 - \frac{C_4}{2(1 + l)^{3/2}}\right] - \frac{3C_2}{2(1 + l)^{5/2}}$$

$$\left[C_3 l + \frac{C_4}{(1 + l)^{1/2}}\right] = 0 \tag{7}$$

where $C_1 = \sqrt{2\varepsilon_0/\pi}$, $C_2 = \sqrt{1 + \mu^2} - \mu$, $C_3 = 0.23$, and $C_4 = 0.577$. Although the angle ψ depends on the angle of loading relative to a crack direction, following the work of Wong in [42], an optimal angle of $\psi = (1/2)\tan^{-1}(1/\mu)$ is chosen.

The second step is to determine the compressive strength of an SVE from the strengths of individual cracks contained in it. Within each circular SVE, the microcracks which are contained in or intersect with it are found. These microcracks are shown in Fig. 3. For each of these cracks s_c is obtained from (5). For cracks which are partially contained within the SVE, only the crack length $2a$ contained within the SVE is processed. The minimum fracture strength is then calculated. As mentioned in Section 2.2, the fracture strength of each SVE is assigned to its centroid to form a uniform grid of mesoscopic fracture strengths as shown in Fig. 1(c).

When an SVE contains no microcracks, a maximum fracture strength based on the minimum half crack length a' is assigned to the SVE; *cf.* Section 2.1. As will be observed in Section 3, in general this maximum strength is assigned to only a very few SVEs, except when a combination of low crack density and small SVE size is used. The SVEs with the assigned maximum strength are not deemed to greatly influence fracture response, as fracture is mostly affected by regions with lower strength. However, to better represent the strength of these SVEs one could consider failure in the bulk and the effect of microcracks, voids, and defects at scales smaller than those considered herein.

2.4. aSDG method and fracture model

The h-adaptive *asynchronous Spacetime Discontinuous Galerkin* (aSDG) method, formulated for elastodynamic problem in [45,46], is utilized for the dynamic fracture simulations. The aSDG method directly discretizes spacetime using nonuniform grids that satisfy a special causality constraint resulting in unique properties, such as a local and asynchronous solution scheme, arbitrarily high and local temporal order of accuracy, and linear solution scaling versus number of elements.

On fracture surfaces often a cohesive model [56,57] is employed to represent the process of debonding. In lieu of such models, we employ an interfacial contact and damage model [58], wherein internal parameters including a damage parameter D model the processes of debonding and contact–stick/ contact-slip mode transitions. On an arbitrary oriented fracture surface, an *effective stress* scalar value drives damage evolution. The effective stress combines positive normal (*i.e.* tensile) and shear traction components and is compared against an *effective fracture strength* $\tilde{s}$ at a given point. The strength field $\tilde{s}$ can be inhomogeneous; in Section 4, it will be discussed how it is derived from a mesoscopic uniaxial compressive strength field, such as that shown in Fig. 1(c).

Fig. 1(d) shows a sample front mesh (spatial mesh) for a dynamic fracture simulation. For each of the vertices of the front mesh, we check if the effective stress exceeds $\tilde{s}$ for any potential angle of crack propagation, $\theta \in [0, 2\pi]$. If so, a crack is nucleated and propagated in that direction. The same holds for the tips of already propagated cracks. Advanced mesh adaptive operations in spacetime are employed to align inter-element boundaries with the proposed crack direction. To further enhance the accuracy and efficiency of the method, an h-adaptive scheme adjusts element sizes in spacetime to satisfy error indicators in the bulk and on fracture interfaces for controlling the energy dissipation and satisfaction of fracture constitutive relations [59]. The combination of these two sets of mesh adaptive operations and aSDG properties enables accurate representation of very complex fracture patterns for dynamic brittle fracture, as shown in Fig. 1(d). For a review of these mesh adaptive operations for fracture analysis, we refer the readers to [21].

The aforementioned adaptive operations accommodate crack propagation in arbitrary directions, thus providing the same or higher flexibility than other mesh adaptive finite element methods [60–63], such as the *eXtended Finite Element Methods* (XFEMs) [64–66] and *Generalized Finite Element Methods* (GFEMs) [67,68], in accurate numerical modeling of complex crack paths. However, there are several advantages to directly aligning element boundaries with crack direction, rather than having cracks go through elements as in XFEMs and GFEMs. Since the elements containing cracks and crack tips require enrichment functions, the finding of such functions can be challenging for XFEMs and GFEMs. For example, the majority of these methods are based on the *Linear Elastic Fracture Mechanics* (LEFM) theory and using nonlinear models such as cohesive and interfacial damage models (used in this manuscript) is cumbersome, at least in elements containing crack tips. Moreover, geometric complexities such as crack branching, microcracking, and crack intersection are very common in dynamic fracture. Again, specific enrichments should be used for such fracture patterns with XFEMs and GFEMs. In contrast, any fracture model can be used between element boundaries and the aSDG mesh adaptive operations can accommodate aforementioned dynamic fracture patterns. However, as discussed in [69], extension of mesh adaptive methods to 3D for aSDG would be more difficult than XFEMs and GFEMs. Finally, we note that meshless methods such as [70] can be appropriate choices for modeling complex rock fracture problems in 2D and 3D.

3. Results for mesoscopic fracture strength homogenization

In this section, the numerical results corresponding to the two scale fracture analysis scheme in Fig. 1 are presented. First, the statistics and initial results from the Yuen-Long marble sample with a Power-Law microcrack distribution and the various generated Weibull distributions with four different shape parameters will be presented in Sections 3.1 and 3.2. Then, the generated Weibull distributions will be analyzed with a specific focus on SVE size in Section 3.3 and a focus on crack density in Section 3.4. Finally, the dynamic fracture analysis performed utilizing the aSDG method are presented in Section 4. The use of the aSDG method is motivated by employing an interfacial contact-damage model and observing complex fracture intersection patterns, *cf.* Fig. 23; otherwise, as discussed in Section 2.4, these aspects pose challenges to methods such as XFEMs and GFEMs.
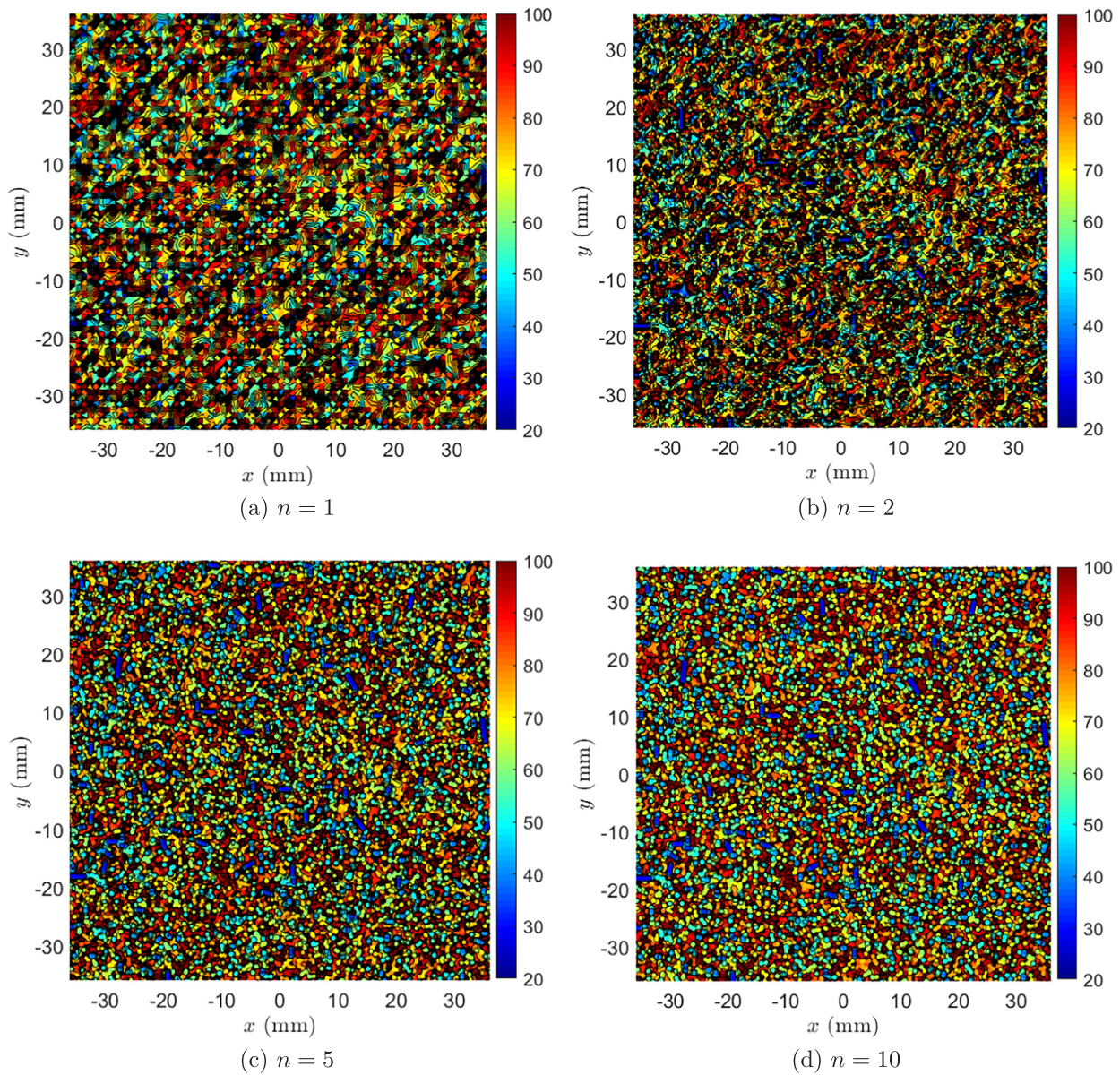
Fig. 6. The effect of SVE spacing n on mesoscopic strength contours s_c for $L_{SVE} = 1$ and $\varepsilon_0 = 0.243$.

(a) $n = 1$

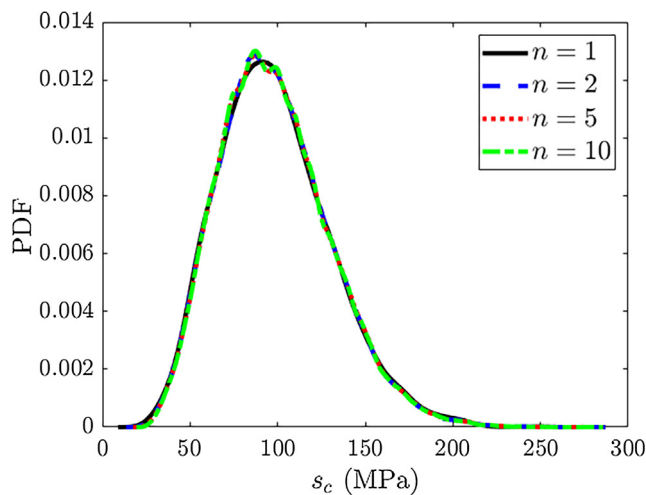(b) $n = 2$

(c) $n = 5$

(d) $n = 10$

Fig. 7. Mesoscopic strength s_c (MPa) PDF for various SVE spacing n ($L_{SVE} = 1$ and $\varepsilon_0 = 0.243$).

3.1. Power and Weibull generated domain results

Six Yuen-Long marble samples were analyzed in [43]. For this analysis, the white marble sample statistics from the sample designated S19 were used to generate the simulated Power-Law domain. Table 1 summarizes the material properties taken from [43]. These properties include the material density ρ, Poisson's ratio ν, Young's modulus E, mean crack length $2a$, characteristic minimum length a', crack density ε_0, Cauchy distribution exponent z, and power law distribution parameter $q*V_0$. The characteristic minimum length a' is also used in the SVE analysis process to calculate the maximum possible strength associated with the minimum potential crack length.

Several Weibull distributions were created with the same mean crack length $2a$ as the power law distribution domain for the Yuen-Long marble sample, 0.141 mm. The goal of this analysis is to show the effect of changing the crack length probability density function (PDF) on the fracture response of the material. Therefore, a wide variety of PDF shapes were required to provide the desired impact on the fracture response. Because the Weibull distribution PDF shape changes drastically with increasing shape parameter m, the m values of $\frac{1}{2}$, 1, 2, and 4
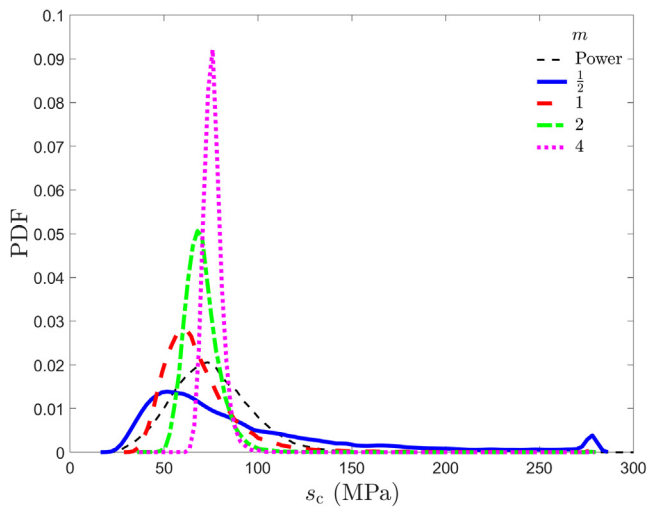
Fig. 8. Mesoscopic strength s_c (MPa) probability density function for power and Weibull distribution domains with $L_{SVE} = 1$ and $\varepsilon_0 = 0.243$.

were selected to change the shape of the distribution. The value of $m = \frac{1}{2}$ provides a PDF shape that is very close to the power-law distribution, while the shape becomes more bell-shaped and less skewed as higher m values such as $m = 4$ are used. The minimum crack length $2a$

of 0.015 mm was kept the same, while also reusing the same Young's modulus and Poisson's ratio. Thus, the Weibull distribution parameter γ was set equal to 0.015, while the r factor was set to unity, since the volume element considered is equal to 32 mm × 32 mm square used in [43] for V_0 ($r = V/V_0 = 1$). The scale parameter η was changed for each m value to maintain the mean crack length of 0.141 mm.

To perform a study of the effect of crack density on mesoscopic fracture strength, three different crack densities ε_0 were analyzed using the Weibull distribution, 0.05, 0.243, and 0.75. Thus a total of 12 individual randomly generated microcracked domains similar to Fig. 1(a) were generated for the Weibull model (four m values times three crack densities). Finally, to show how small and large SVE sizes capture the heterogeneities in the microcrack-filled domain, we determine macroscopic fracture strength of each of these 12 RVEs with different SVE sizes of L_{SVE} equal to 1, 2, 4, and 8 mm. Thus, the analyses for the Weibull model involves 12 distinct microcracked domain resulting in 48 mesoscopic fields for s_c.

As shown in Fig. 1(a) microcracks are formed in a 80 mm × 80 mm square domain centered at (0, 0). Four of the twelve generated Weibull distribution microcrack domains analyzed with $\varepsilon_0 = 0.243$ are shown in Fig. 4. Fig. 5 shows the corresponding crack length probability density functions. For the Weibull distributions, $m = \frac{1}{2}$ most closely approximates the power law distribution. As m increases, the shape changes such that there are less smaller cracks and a more defined bell-curve shape that results in a smaller standard deviation of length for the distribution is formed.
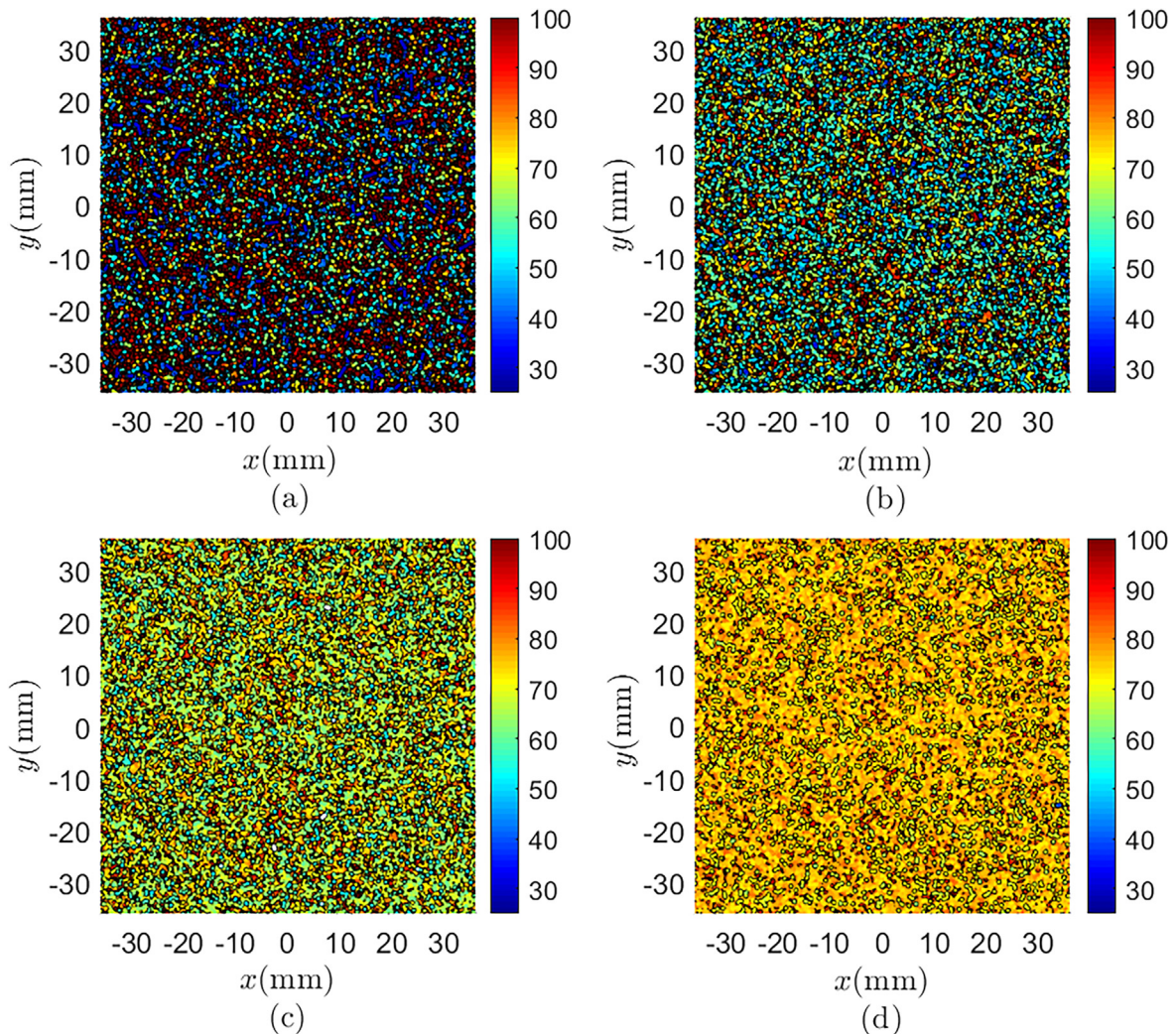

Fig. 9. Mesoscopic strength contour s_c (MPa) for $\varepsilon_0 = 0.243$, $L_{SVE} = 1$, and Weibull shape parameters (a) $m = \frac{1}{2}$, (b) $m = 1$, (c) $m = 2$, and (d) $m = 4$.
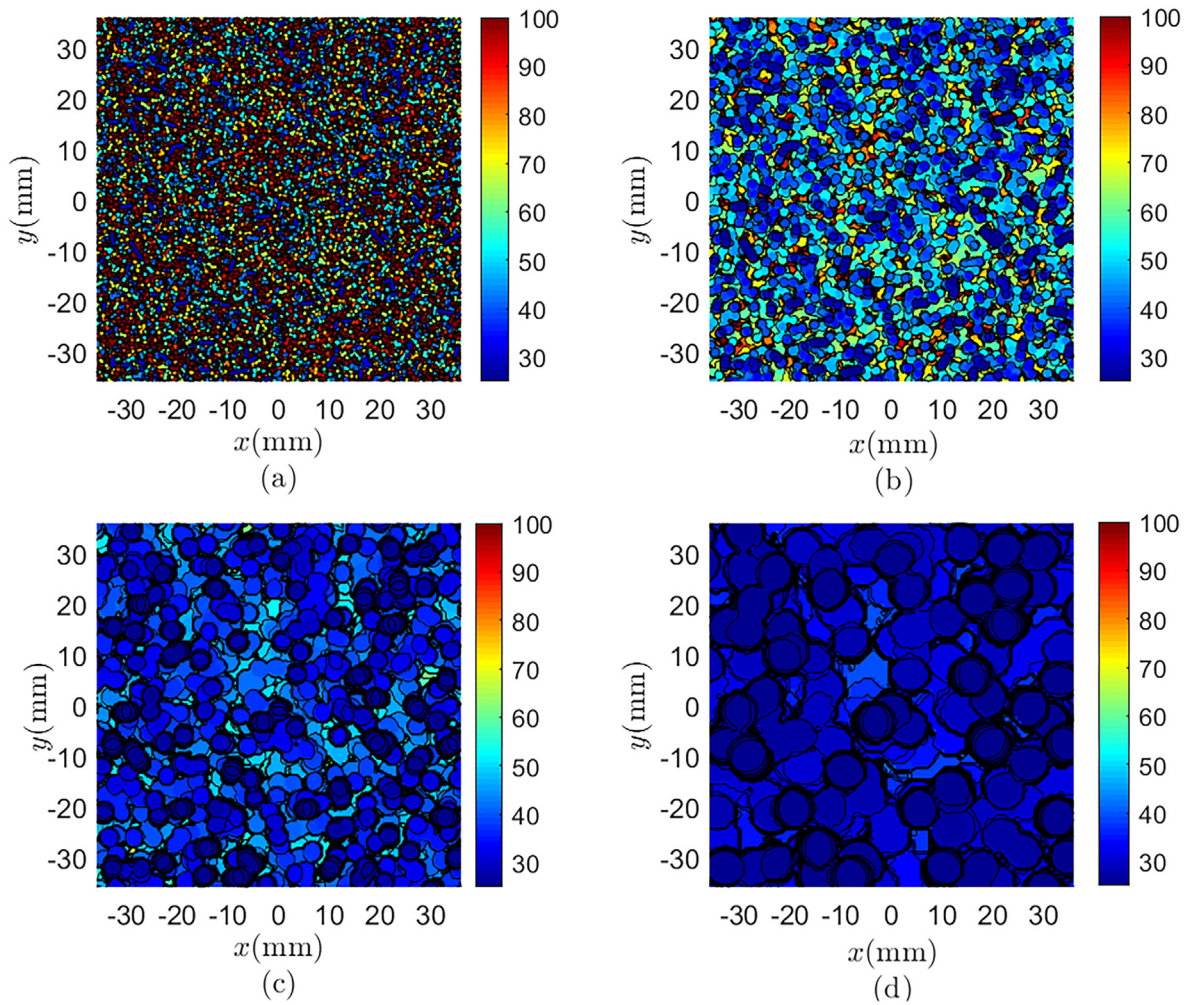
Fig. 10. Mesoscopic strength contour s_c (MPa) SVE size effect comparison for $\varepsilon_0 = 0.243$, $m = \frac{1}{2}$, with (a) $L_{SVE} = 1$, (b) $L_{SVE} = 2$, (c) $L_{SVE} = 4$, and (d) $L_{SVE} = 8$.

Before performing the SVE analysis process, a reasonable value for SVE spacing, equal to $n = 10$, is determined and detailed next in Section 3.1.1. Each domain is then analyzed using SVEs with the proper spacing. For each SVE a uniaxial compressive strength was assigned based on the minimum values of strength calculated for the microcracks in the SVE. For SVEs with no microcrack a crack with minimum length of 0.015 mm is considered; *cf.* the discussion at the end of Section 2.3. The contour plot of strengths for the power law distribution with $L_{SVE} = 1$ and $n = 10$ is shown in Fig. 6(d). After calculating the strength field, the strength field statistics are calculated to provide a better understanding of the general strength trends based on the three different variables that were changed: distribution type and shape, L_{SVE} size, and crack density.

3.1.1. Effect of SVE spacing

As discussed in Section 2.2, in moving window method the RVE is traversed with SVEs with spacing S. In order to determine a reasonable value for this spacing, four values of $n = 1, 2, 5, 10$ were chosen. For lower values of n, the analysis loses spatial resolution, and may not even completely cover the RVE ($n = 1$), leading to gaps that may miss certain cracks entirely. For higher values of n, the statistical distribution of calculated fracture strengths do not vary much with increasing spatial resolution, resulting in a greater computational cost for no apparent gain in creating the mesoscopic fracture strength field. This trend is shown in Fig. 6 in the strength contour plots. The PDFs of strength for various n, and for $L_{SVE} = 1$, in Fig. 7 show that there is not a large difference in strength statistics even with the smallest $n = 1$ is used. The

mean strength of the field does change slightly with greater n values, converging to the true value with a smaller spacing between each SVE. For the rest of this manuscript, the value $n = 10$ was selected for calculating the SVE spacing $S = L_{SVE}/n$ as the best trade-off between spatial resolution and computational cost.

3.2. Distribution type and shape effect

The goal of this section is to demonstrate how the shape of the distribution of cracks at the microscale affects the statistics of mesoscopic strength field. This is facilitated by using different shape parameters for synthetic Weibull distributions; *cf.* Section 2.1. The data shown in the strength probability density function, found in Fig. 8, is in agreement with the expected trends after reviewing the crack length probability density function in Fig. 5. Despite each domain containing the same mean crack length, the actual mean strength does vary depending on the crack length distribution shape. The variance that results is a function of the fact that the $m = \frac{1}{2}$ and $m = 1$ distributions contain a larger standard deviation, with a larger number of both smaller and larger cracks about the average than the more bell-curve shape crack length distributions for $m = 2$ and 4. This feature can also be shown by reviewing the strength contours themselves for each of various m shapes, as seen in Fig. 9.

Due to a feature of the SVE averaging process wherein any empty SVEs are assigned a strength for a crack of a minimum length, the probability density function that results from this analysis with the smaller L_{SVE} sizes inevitably appears bi-modal with two primary modes:
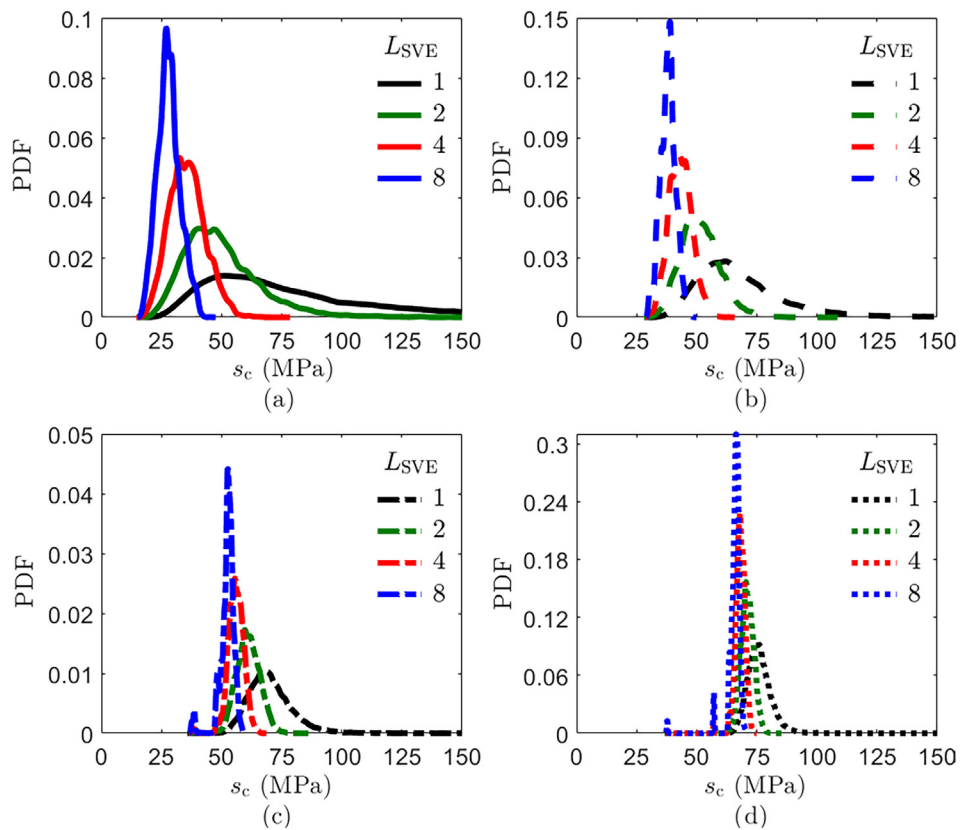
Fig. 11. Strength probability density function and SVE size effect comparison for $\varepsilon_0 = 0.243$, with (a) $m = \frac{1}{2}$, (b) $m = 1$, (c) $m = 2$, and (d) $m = 4$.
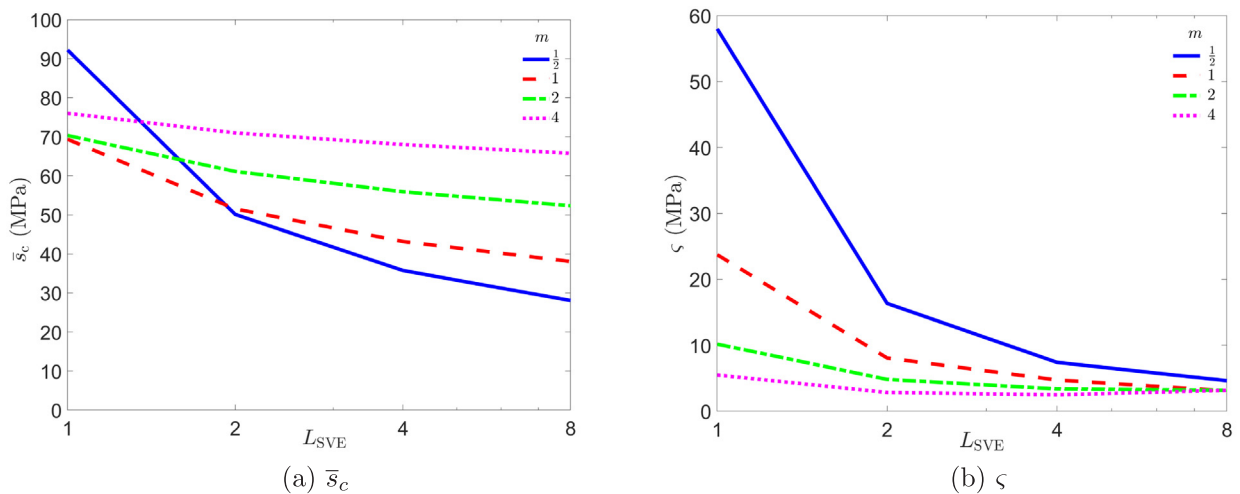

Fig. 12. Mean strength $\bar{s}_c$ and standard deviation ς for $\varepsilon_0 = 0.243$.

one lower strength mode for the SVEs which contain cracks, and a smaller, higher strength mode for the few SVEs without any crack interaction. As would be expected, utilizing larger SVE sizes removes this feature, as there are fewer SVEs and therefore a reduced number or no SVEs without any cracks containing within the SVEs. This will be detailed in the next section, Section 3.3. For the power law distribution, the calculated mean strength for $L_{SVE} = 1$ is 72.67 MPa, slightly higher than the sample material strength of 55.85 MPa reported in [43]. This is a result of considering both the empty and non-empty SVEs. It is noted that from the Weibull distribution results, those corresponding to $m = \frac{1}{2}$ are the most realistic, as its microcrack length distribution in Fig. 5 (and consequently s_c in Fig. 8) are closest to that of the power distribution for this Yuen-Long marble sample.

3.3. Weibull distribution comparison: SVE size effect

The size of the SVE, L_{SVE}, strongly controls the statistics of the heterogeneous fracture strength field averaged, such as its point-wise *Probability Distribution Function* (PDF). Recall the parameter β, equal to $L_{SVE}/\mathbb{E}(2a)$, from Section 2.2; as this parameter (*i.e.* the SVE size) tends to infinity, the material inhomogeneity is lost for this macroscopically homogeneous rock. To show this *size effect*, four different L_{SVE} sizes were used: 1, 2, 4, and 8 mm.

Fig. 10 shows the strength contour plots of the same domain ($m = \frac{1}{2}, \varepsilon_0 = 0.243$) for each of the various SVE sizes. Each of the four individual subplots utilize the same contour range, which allows for objective comparison of strength fields across each plot. The smaller
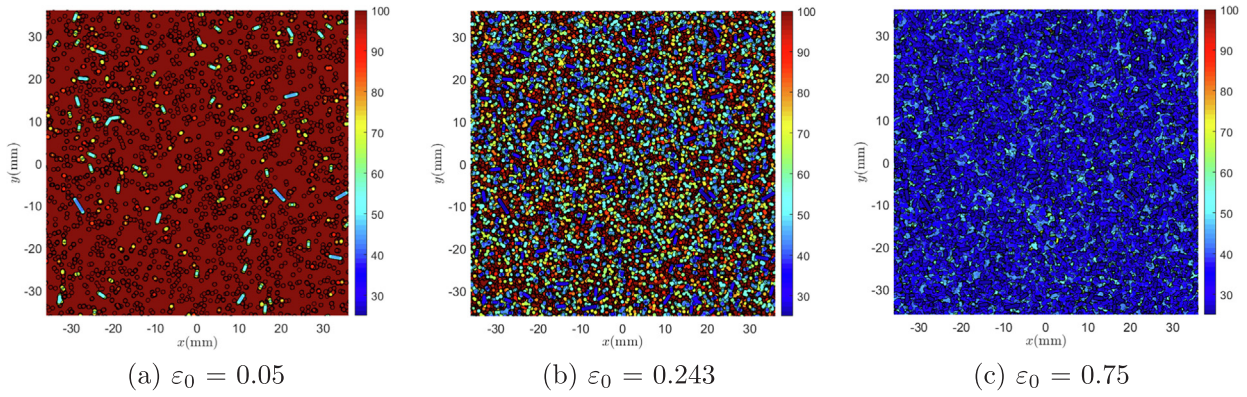
(a) $\varepsilon_0 = 0.05$　　　　　　　　(b) $\varepsilon_0 = 0.243$　　　　　　　　(c) $\varepsilon_0 = 0.75$

Fig. 13. Mesoscopic strength s_c contours for $m = \frac{1}{2}$, (a) $\varepsilon_0 = 0.05$, (b) $\varepsilon_0 = 0.243$, and (c) $\varepsilon_0 = 0.75$.
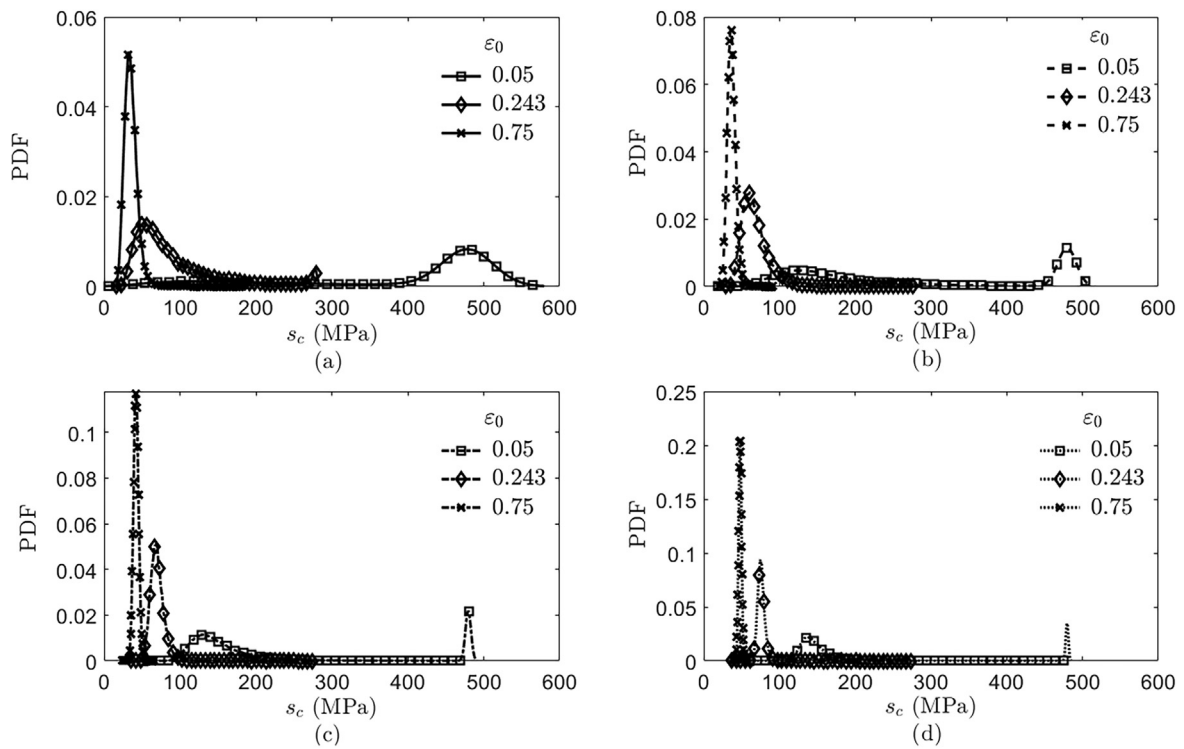
Fig. 14. Strength probability density function comparison for various crack densities and Weibull distribution shape parameters for $L_{SVE} = 1$, (a) $m = \frac{1}{2}$, (b) $m = 1$, (c) $m = 2$, and (d) $m = 4$.

(a) Structured 360×360 grid for fracture strength

(b) Initial unstructured spatial mesh for aSDG fracture analysis

(c) Interpolation of properties at quadrature points

Fig. 15. Distinct discrete grids for material properties and fracture analysis.

Fig. 16. Applied boundary conditions for aSDG dynamic fracture analysis.
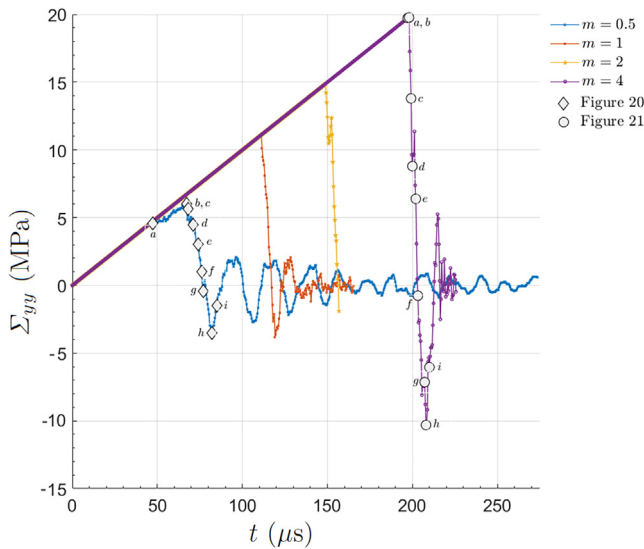
Fig. 17. Macroscopically homogenized stress Σ_{yy} versus time for all Weibull distributions. The detailed solution for different stages of solutions for $m = \frac{1}{2}$ and 4 are shown in Figs. 21 and 22, respectively.

Fig. 18. Macroscopically homogenized strain E_{yy} versus stress Σ_{yy} for all Weibull distributions.

Table 2
Important quantities of macroscopic tensile strain-stress response in *y* direction.

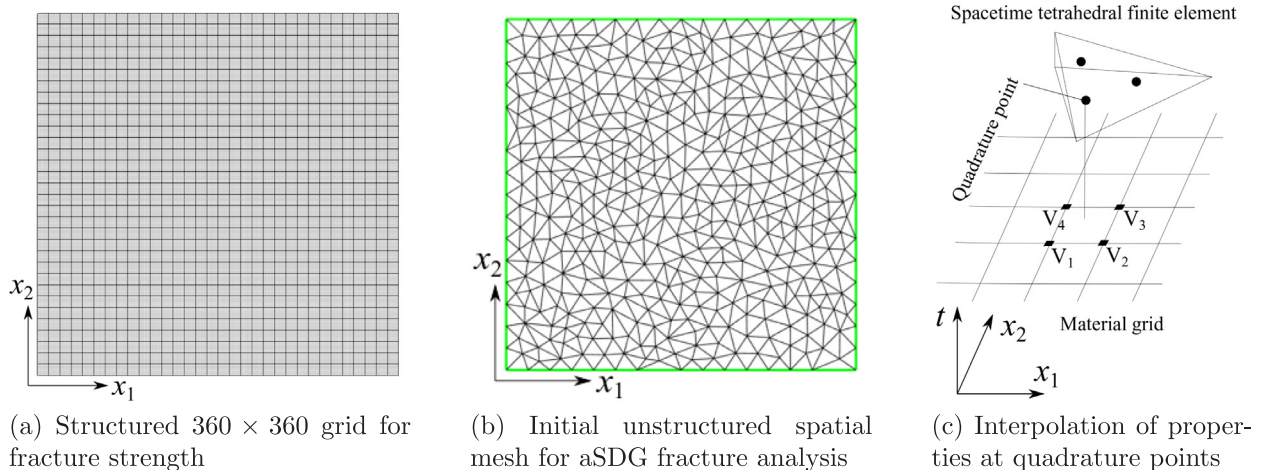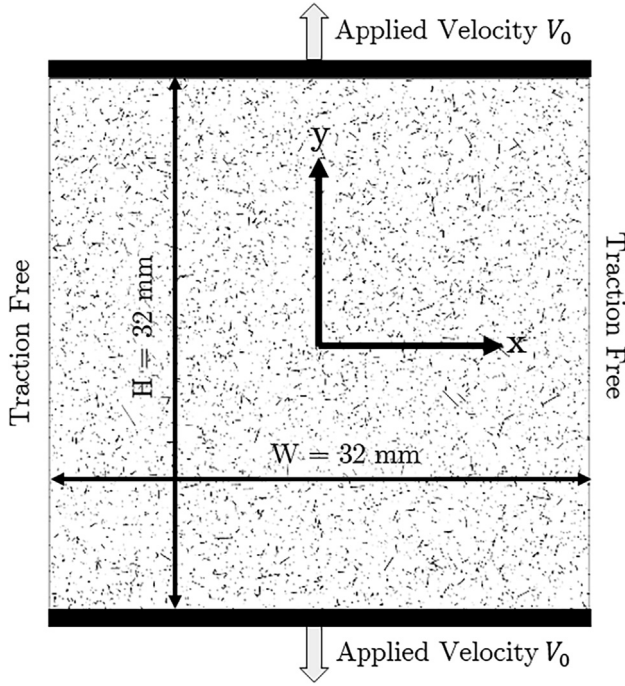|	m	$\frac{1}{2}$	1	2	4
Initiation of nonlinear response	$\widetilde{t}_i$ (μs)	46	110	130.8	197.2
	$\widetilde{E}_i$	6.44×10^{-5}	1.54×10^{-4}	1.83×10^{-4}	2.76×10^{-4}
	$\widetilde{\Sigma}_i$ (MPa)	**4.60**	**11.0**	**13.1**	**19.7**
	$\widetilde{\psi}_i$ (J/m³)	148	847	1199	2719
Maximum stress	$\widetilde{t}_m$ (μs)	67.2	111.2	148.8	198
	$\widetilde{E}_m$	9.41×10^{-5}	1.56×10^{-4}	2.08×10^{-4}	2.77×10^{-4}
	$\widetilde{\Sigma}_m$ (MPa)	**6.0**	**11.1**	**14.9**	**19.8**
	$\widetilde{\psi}_m$ (J/m³)	351	921	1666	2832
Failure	$\widetilde{t}_f$ (μs)	76.7	117.2	156.4	203.0
	$\widetilde{E}_f$	1.07×10^{-4}	1.64×10^{-4}	2.19×10^{-4}	2.84×10^{-4}
	$\widetilde{\psi}_f$ (J/m³)	**530**	**1124**	**2210**	**3297**
Brittleness factors	$\widetilde{t}_i/\widetilde{t}_f = \widetilde{E}_f/\widetilde{E}_i$	0.60	0.94	0.84	0.97
	$\widetilde{\psi}_i/\widetilde{\psi}_m$	0.42	0.92	0.72	0.96
	$\widetilde{\psi}_m/\widetilde{\psi}_f$	0.66	0.82	0.75	0.86

SVE size, $L_{SVE} = 1$, contains a multitude of high and low strength SVEs. As the SVE size increases, the strength in the field becomes lower and more homogeneous.

The strength PDFs in Fig. 11 show the same trends for each m value for the various Weibull distributions. The change of mean ($\bar{s}_c$) and standard deviation (ς) of strength versus SVE size are also shown in Fig. 12. As m increases, the mean strength generally increases. The only exception is $L_{SVE} = 1$ and $m = \frac{1}{2}$, as shown in Fig. 12(a). This is due to the wide span of crack lengths allowed by this distribution. Generally, the majority of the cracks for this distribution are extremely small. However, larger cracks are allowed, which results in an extremely high standard deviation. Moreover, as shown in Fig. 12(a), $\bar{s}_c$ decreases when L_{SVE} increases. This well-known *size effect* for quasi-brittle materials is contributed to the fact that larger SVEs contain more microcracks thus
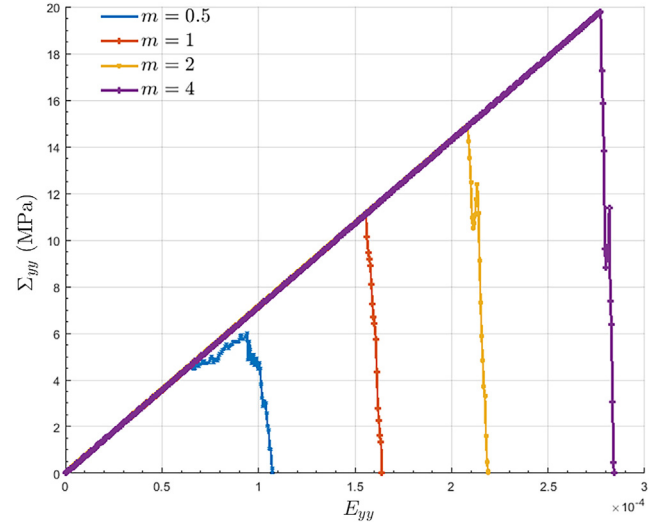
are more likely to contain longer cracks. This results in lower mean strengths for larger SVEs.

As the size of the SVE increases, the standard deviation ς tends to zero. The decreased variation of the field is shared among all fields homogenized/ averaged by SVEs, since as larger SVEs are considered the population of microstructural features (microcracks herein) increases and their statistic converges to that of the macroscopic domain. From Fig. 12(a), the crack length Weibull shape parameter m has no major impact on small values of ς for large SVE sizes. The mean strength $\bar{s}_c$ of the field still strongly depends on the actual crack distribution shape m even at larger SVE sizes, due to the differences in the allowable crack lengths.

Maintaining rock inhomogeneity is advantageous for fracture analysis of quasi-brittle materials, particularly under loading scenarios where there is no macroscopic stress concentration points; *i.e.* similar to problems considered in Section 4. This analysis shows the importance of maintaining a relatively small SVE size to increase the fidelity of fracture simulations using the corresponding homogenized strength field. Consequently, as long as smaller SVEs are representative, they are preferred for fracture analysis.
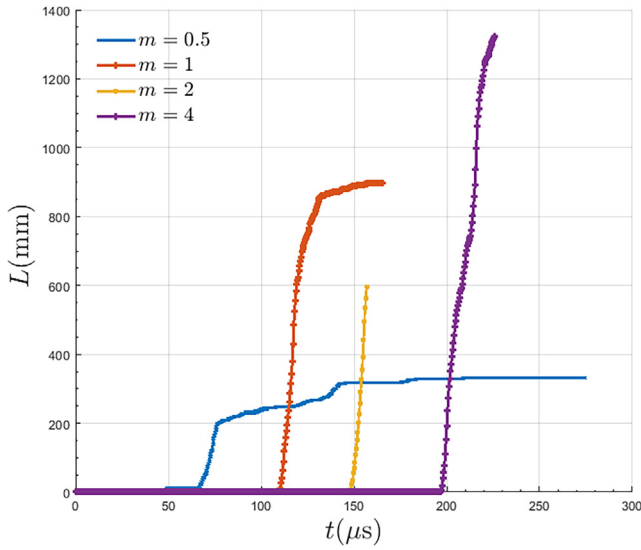
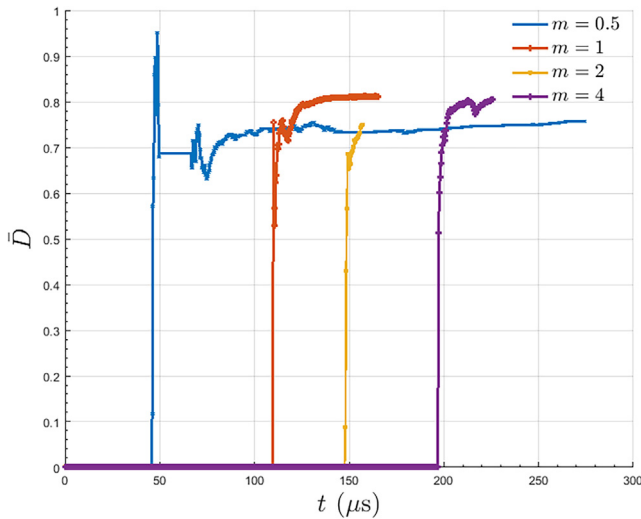**Fig. 19.** Total crack length L versus time for all Weibull distributions.

Fig. 20. Averaged damage parameter $\overline{D}$ versus time for all Weibull distributions.

3.4. Weibull distribution comparison: crack density effect

The actual Yuen-Long marble sample statistics were utilized to generate domains with crack density $\varepsilon_0 = 0.243$ in preceding sections. However, the domains in this section are computationally created with different crack densities to investigate its effect on the statistics of mesoscopic strength. The sliding wing-crack model contains a variable y that attempts to take into account the effect of crack interaction on the fracture strength based on the crack density. A low crack density of $\varepsilon_0 = 0.05$ and a high crack density of $\varepsilon_0 = 0.75$ were selected along with $\varepsilon_0 = 0.243$ for this analysis. Solving Eq. (6) results in $y = 0.37$, 0.64, and 0.96 for $\varepsilon_0 = 0.05$, 0.243, and 0.75, respectively. This modifies the fracture strength in Eq. (5), with a higher crack density resulting in a lower overall strength, as would be expected.

Fig. 13 shows the strength contours for $m = \frac{1}{2}$ with varying ε_0. For low density $\varepsilon_0 = 0.05$, the strength field has a nearly uniform high strength. The (longer) cracks that are placed in the domain are easily seen in the strength contour, as the sampling SVEs at the grid points effectively expand them by a thickness proportional to the SVE size. The resulting PDF in Fig. 14 is bi-modal due to the large number of SVEs that do not contain a crack. Comparatively, the higher density $\varepsilon_0 = 0.75$

is almost uniformly lower in strength. As the crack density increases, this bi-modal feature of the crack field for the SVE averaging process is reduced. These results show that the crack density affects at what size the SVE can be considered representative, *i.e.* the majority of sampled SVEs containing cracks. For example, for $\varepsilon_0 = 0.05$ SVEs with $L_{SVE} = 1$ are not appropriate due to the large number of empty SVEs resulting in the bi-modal shape for the PDF in Fig. 13(a). It is noted that the low density of $\varepsilon_0 = 0.05$ is intentionally chosen to better demonstrate that L_{SVE} cannot be set to arbitrarily small values. For domains with a higher crack density, *i.e.* experimentally observed $\varepsilon_0 = 0.243$, $L_{SVE} = 1$ is deemed representative and from this perspective even smaller SVEs can be considered to better capture rock inhomogeneity. Finally, it is noted that strength steadily decreases as the crack density increases. This is similar to the effect that increasing SVE size has, because in both cases more cracks are sampled within an SVE, thus reducing the (mean) averaged fracture strength of SVEs.

4. Macroscopic fracture analysis

4.1. Problem description

As shown in Fig. 1(c), from the averaging scheme discussed in previous sections, a structured grid of s_c is formed for macroscale fracture analysis. To study the effect of changing shape parameter m for the Weibull distribution, four different simulations were performed for each m value. For these simulations we use strength fields obtained by SVE size $L_{SVE} = 1$ since they retain the most heterogeneity. The crack density is $\varepsilon_0 = 0.243$. The four employed fields for s_c are shown in Fig. 9.

Fig. 15 shows two different grids employed for storing fracture strengths and fracture analysis. As will be discussed below, the 32 mm × 32 mm RVE shown in Fig. 1(a) is subject to a vertical uniaxial tensile loading. Since the grid spacing is $L_{SVE}/n = 0.1$ ($n = 10$; *cf.* Section 2), fracture strengths in Fig. 9 are stored in a 360 × 360 structured grid shown in Fig. 15a. The initial spatial mesh for fracture analysis, containing 803 triangular space elements is shown in Fig. 15b. Since the aSDG directly discretizes space and time, for a spatially 2D problem, the computational domain is three dimensional in spacetime. Accordingly, the aSDG method builds a spacetime mesh of tetrahedral elements, by pitching vertices of this mesh in time; *cf.* Section 2.4 and [71,45]. Mesh adaptive operations adjust the space mesh to first ensure solution is captured with sufficient accuracy and second align element boundaries with proposed crack directions, so that fracture pattern is accurately captured. An intermediate front mesh for a dynamic fracture analysis is shown in Fig. 1(d). As can be seen, the elements in the front mesh are finer close to fractures (blue to red thick lines) in response to the two adaptive operations discussed above.

The spacetime elements of the aSDG method are tetrahedra attached to this spatial front. Since the spatial front adapts in response to the ever evolving fracture pattern, the spatial location of the quadrature points of the spacetime elements varies. As shown in the zoomed view Fig. 15c, a sample quadrature point is spatially contained in one square of the uniform material grid with vertices V_1 to V_4. Fracture strength at this point is obtained by linear interpolation of mesoscopic strength values stored at vertices V_1 to V_4.

If elastic properties were also deemed to be inhomogeneous, they would be stored in the material mesh and obtained by the same process. However, homogeneous and isotropic elastic material properties for rock are taken from Wong [43] for material sample S19: Young's Modulus $E = 65$ GPa, mass density $\rho = 2700 \frac{\text{kg}}{\text{m}^3}$, and Poisson's ratio $\nu = 0.3$. A 2D plane strain condition is assumed for the analysis. A displacement solution in the form,

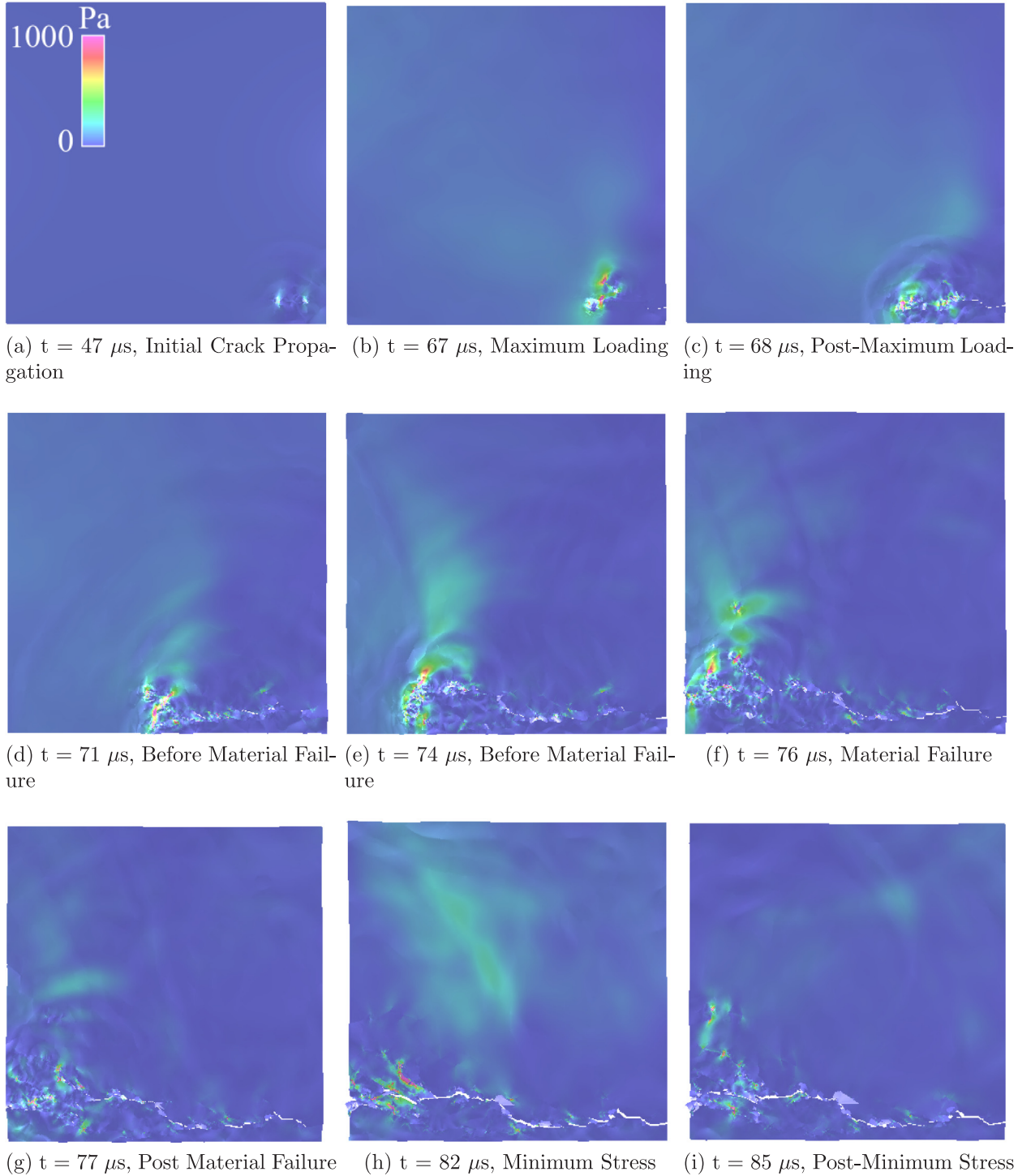$$u_x = axt \tag{8a}$$

$$u_y = byt \tag{8b}$$

(a) t = 47 μs, Initial Crack Propagation

(b) t = 67 μs, Maximum Loading

(c) t = 68 μs, Post-Maximum Loading

(d) t = 71 μs, Before Material Failure

(e) t = 74 μs, Before Material Failure

(f) t = 76 μs, Material Failure

(g) t = 77 μs, Post Material Failure

(h) t = 82 μs, Minimum Stress

(i) t = 85 μs, Post-Minimum Stress

Fig. 21. aSDG solution visualization for Weibull shape parameter $m = \frac{1}{2}$. Color and height fields depict internal and kinetic energy densities, respectively. (For interpretation of the references to color in this figure legend, the reader is referred to the web version of this article.)

satisfies the elastodynamic equation of motion. The coefficients a and b are normal strain rates in x and y directions, respectively. The solution (8) corresponds to the velocity field $v_x = ax$, $v_y = by$ and the strain field $\epsilon_{xx} = at$, $\epsilon_{yy} = bt$, $\epsilon_{xy} = 0$. For all values of a and b, the corresponding stress field is spatially uniform and temporally linearly increasing. This type of loading is typical for fragmentation analysis, *e.g.*, [54,21]. In fact, for a material with homogeneous fracture properties, a fracture initiation condition is suddenly satisfied across the whole domain once the stress field becomes sufficiently large to satisfy such condition at any point. This response is clearly non-physical and is avoided herein

by using mesoscopically inhomogeneous fracture strength fields.

By choosing specific values of a and b, confined and unconfined uniaxial and biaxial tensile and compressive loading conditions can be designed. For an unconfined uniaxial loading in direction y, stress components are,

$$\sigma_{xx} = 0, \qquad \sigma_{yy} = \dot{\sigma}t, \qquad \sigma_{xy} = 0, \tag{9}$$

where $\dot{\sigma}$ is a user-specified stress rate. For the plane strain condition, the corresponding coefficients in (8) are $a = -\dot{\sigma}\nu(1 + \nu)/E$ and $b = \dot{\sigma}(1 - \nu)(1 + \nu)/E$. Herein, we choose the stress rate $\dot{\sigma} = 10^{11}$ Pa/s.
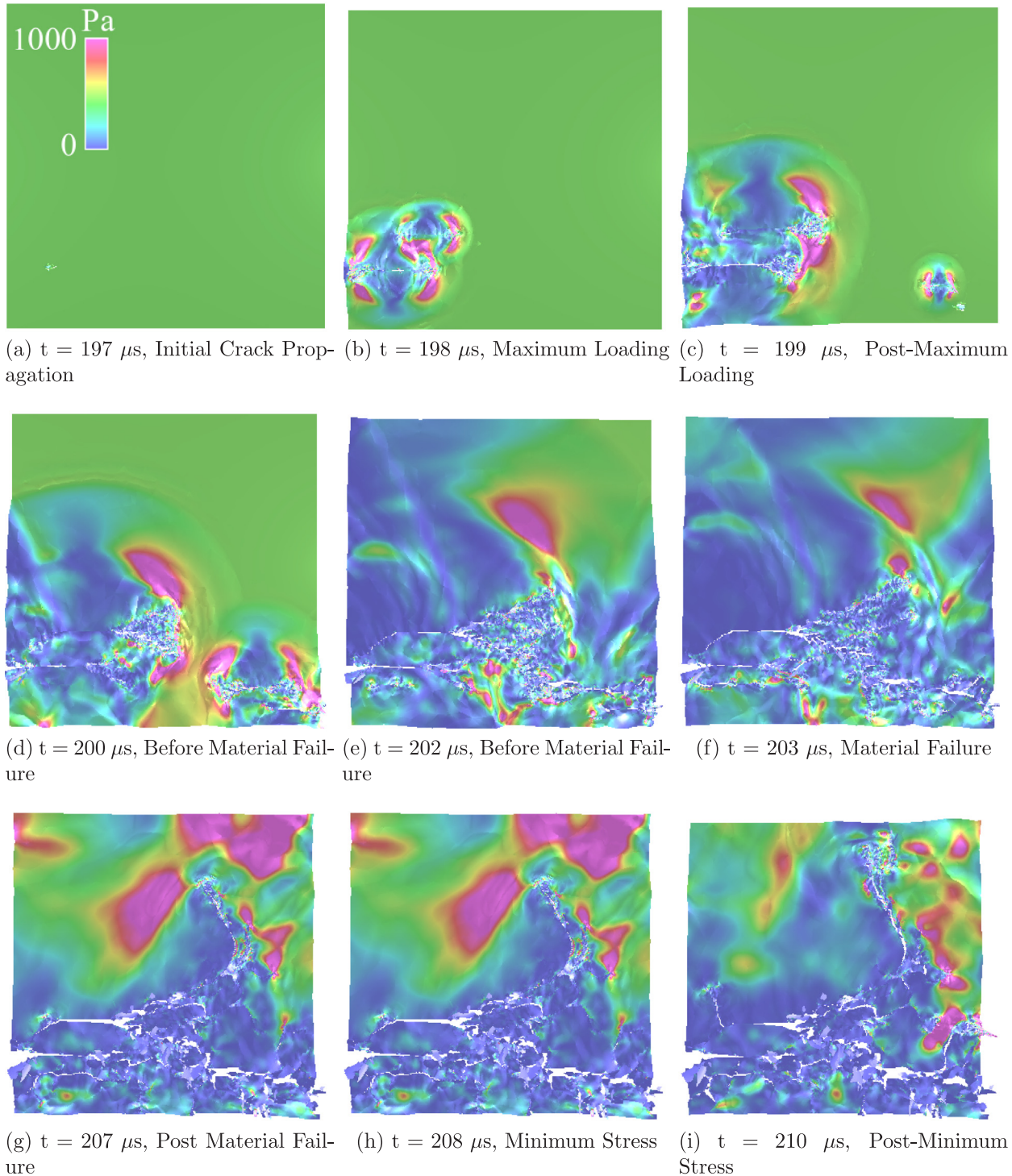
(a) t = 197 μs, Initial Crack Prop- (b) t = 198 μs, Maximum Loading (c) t = 199 μs, Post-Maximum
agation   Loading

(d) t = 200 μs, Before Material Fail- (e) t = 202 μs, Before Material Fail- (f) t = 203 μs, Material Failure
ure   ure

(g) t = 207 μs, Post Material Fail- (h) t = 208 μs, Minimum Stress (i) t = 210 μs, Post-Minimum
ure   Stress

Fig. 22. aSDG solution visualization for Weibull shape parameter $m = 4$. Color and height fields depict internal and kinetic energy densities, respectively. (For interpretation of the references to color in this figure legend, the reader is referred to the web version of this article.)

This corresponds to strain rates $a = -0.6$/s and $b = 1.4$/s for $E = 65$ GPa and $\nu = 0.3$. That is, displacement solution in (8) corresponds to a spatially uniform and temporally increasing tensile loading ($\dot{\sigma} > 0$) in vertical direction until the very first crack is nucleated in the macroscopic domain.

The initial and boundary conditions for this problem are set consistent with these solution fields and are shown in Fig. 16. Due to the temporally increasing stress field in (9), eventually a crack is nucleated from the weakest point of the sampled fracture strength field, *cf.* Fig. 15a. In subsequent times, the displacement, velocity, strain, and

stress solutions presented above no longer hold as the propagation of cracks disrupt them. Consistent with the exact solution prior to nucleation of any cracks, we enforce a traction free boundary condition on the vertical boundaries. On top and bottom surfaces we apply zero tangential stress (frictionless condition) and normal velocity $V_0 = bH/2 = 22.4$ mm/s. This resembles a *displacement-control* loading in quasi-static condition and ensures that we capture the unloading part of the macroscopic strain-stress curve through the process of loading and failure of the RVE.

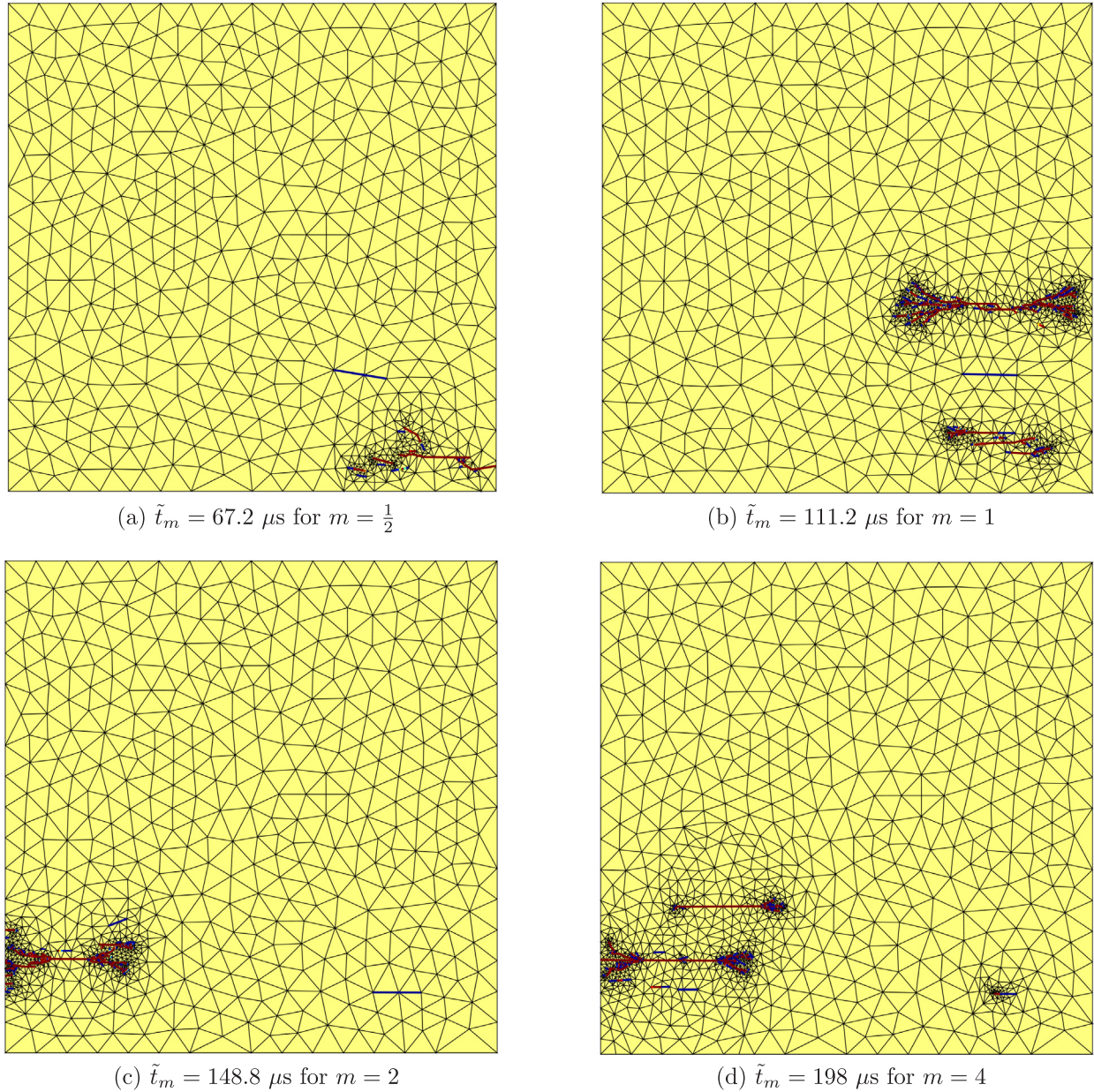In simplest form, a crack nucleation/extension criterion compares a

(a) $\tilde{t}_m = 67.2 \ \mu s$ for $m = \frac{1}{2}$

(b) $\tilde{t}_m = 111.2 \ \mu s$ for $m = 1$

(c) $\tilde{t}_m = 148.8 \ \mu s$ for $m = 2$

(d) $\tilde{t}_m = 198 \ \mu s$ for $m = 4$

Fig. 23. aSDG front meshes for Weibull distributions at maximum stress stage.

scalar *effective* stress s_{eff} formed from the normal t_n and shear t_s components of traction components on a potential crack surface versus an *effective fracture strength* $\tilde{s}$. If at the spatial location $\mathbf{x}$, the condition $s_{\text{eff}}(\mathbf{x}, \theta) \geqslant \tilde{s}(\mathbf{x}, \theta)$ is satisfied for any potential crack extension angle $\theta \in [0, 2\pi]$ in 2D, a crack is nucleated (or extended if $\mathbf{x}$ is already the tip of a propagating crack), along an angle for which $s_{\text{eff}}(\mathbf{x}, \theta)/\tilde{s}(\mathbf{x}, \theta)$ is maximum (and greater than 1). The dependence of $\tilde{s}$ on $\mathbf{x}$ represents an inhomogeneous strength field, whereas anisotropy of strength is incorporated on the dependence of $\tilde{s}$ on θ, an aspect not considered in the present study.

Since the following fracture simulations are for uniaxial tensile loading, we aim to employ an effective stress model that is more appropriate for such loading. The inhomogeneous fields for effective fracture strength $\tilde{s}$ are obtained from the uniaxial compressive strength fields for s_c in Fig. 9. The Mohr-Coulomb failure criterion stipulates a relation between uniaxial tensile and compressive strengths; that is $\tilde{s} = s_c(1 - \sin\phi)/(1 + \sin\phi)$, where $\phi = \tan^{-1}(\mu)$ is the *friction angle*. Similar to [43] we assume the macroscopic friction coefficient to be 0.6

and use the linear relation above to map the compressive strength fields in Fig. 9 to those for $\tilde{s}$. Finally, a shortcoming of the Mohr-Coulomb failure criterion is that it predicts incorrect fracture angles, thus making it inappropriate for tensile fracture simulations. Instead, we employ the *Maximum Circumferential Stress Criterion* (MCSC) [72], where $s_{\text{eff}} = \langle t_n \rangle_+$ and $\langle . \rangle_+$ is the Macaulay positive bracket, ensuring that only tensile traction ($t_n > 0$) contributes to the effective stress. We refer the reader to [22] for the details on this effective stress model and its use by the aSDG method.

4.2. Macroscopic strain versus stress response

The purpose of this example is to demonstrate the great effect of the distribution of microcrack length on macroscopic response. The power law distribution of half crack length for S19 in [43] and all four synthesized Weibull distributions in Fig. 5 have the same mean values. However, they result in different PDFs for mesoscopic strengths in Fig. 8. We use the shape parameter m to demonstrate the great

(a) $\tilde{t}_f = 76.7~\mu$s for $m = \frac{1}{2}$

(b) $\tilde{t}_f = 117.2~\mu$s for $m = 1$

(c) $\tilde{t}_f = 156.4~\mu$s for $m = 2$

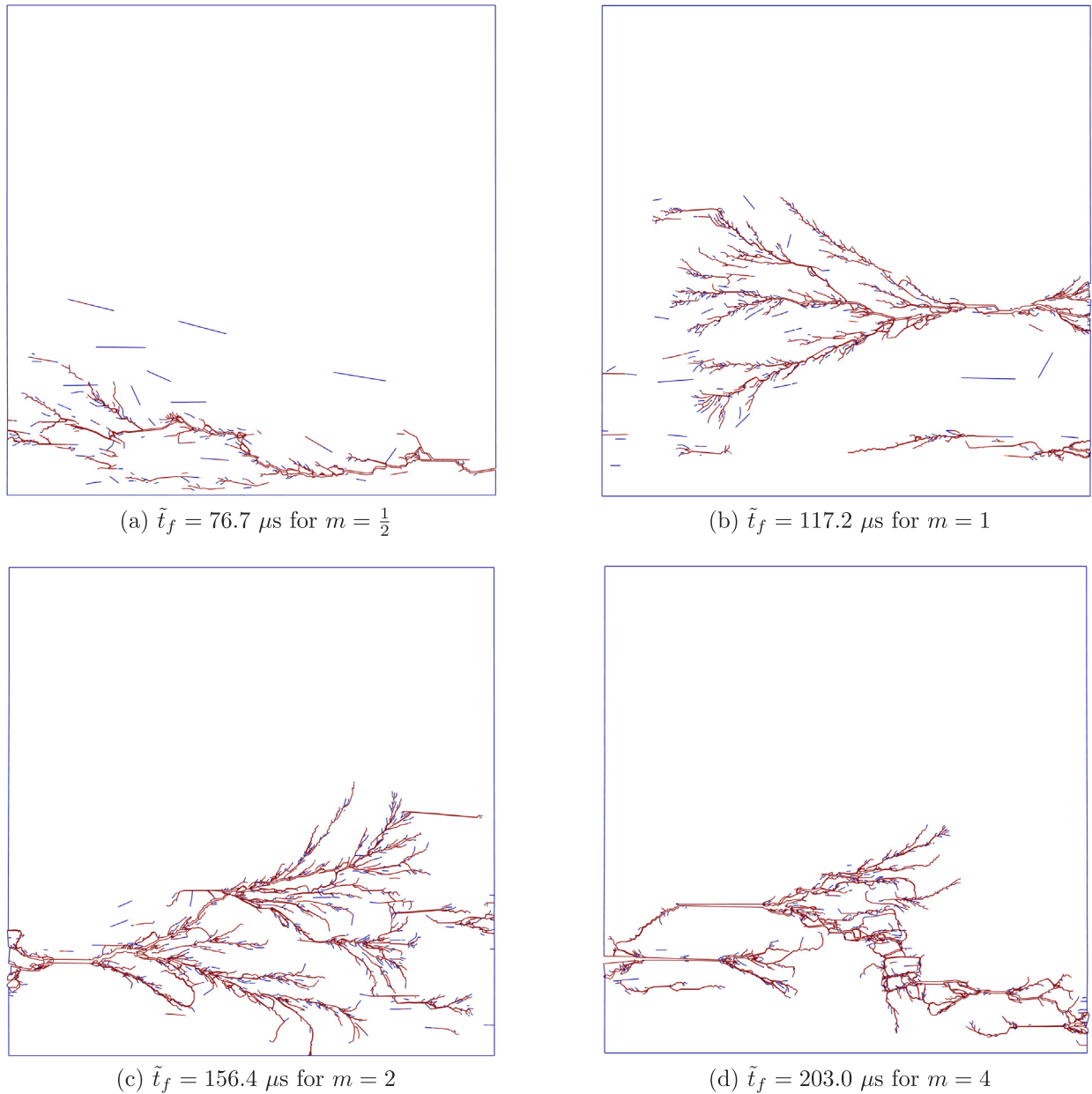(d) $\tilde{t}_f = 203.0~\mu$s for $m = 4$

Fig. 24. aSDG deformed shape for Weibull distributions at failure stage.

influence of the shape of PDF of microcracks on macroscopic response subsequently. By referring to Figs. 5 and 8, it is noted that the results for $m = \frac{1}{2}$ would be the most representative for rock sample S19 in [43] with its power law distribution.

We use homogenization boundary integrals [73] to obtain macroscopic strain E and stress Σ tensors for each instant of the loading for different values of m. These homogenized values correspond to averaged stresses and strains that are applied on the boundary of the 32 mm × 32 mm RVE in Fig. 16. Fig. 17 shows the histories of Σ_{yy} versus time for all Weibull distribution models for microcrack length; since $\Sigma_{xx} = 0$ and $\Sigma_{xy} = 0$ (as expected from problem description), their histories are not presented.

To discuss important stages of strain versus stress response, we focus on the result for $m = \frac{1}{2}$. As shown, up to time $t = \tilde{t}_i = 46~\mu$s, Σ_{yy} linearly increases versus time; cf. (9). At this time, the first cracks are nucleated in the domain due to the increased stress level, resulting in the degradation of rock. This response continues until the maximum stress $\tilde{\Sigma}_m = 6$ MPa is attained at $t = \tilde{t}_m = 67.2~\mu$s. The stress $\tilde{\Sigma}_m$ can be

associated with macroscopic tensile strength of this size of RVE for $m = \frac{1}{2}$. Past time $\tilde{t}_m$, cracks (shown later) have propagated in large portions of the domain. This results in stress unloading until Σ_{yy} reaches zero at $t = \tilde{t}_f = 76.7~\mu$s. Afterwards, some oscillations are observed in stress response due to dynamic nature of the loading and complete failure of the RVE.

The three important points of strain-stress response are: *initiation of nonlinear response*, *maximum stress*, and *failure*. The time ($\tilde{t}$), strain ($\tilde{E}$), stress ($\tilde{\Sigma}$), and energy density ($\tilde{\psi}$) corresponding to these stages are subscripted with i, m, and f, respectively, as observed in the preceding paragraph. Herein, energy refers to the area under the strain-stress curve. Thus, $\tilde{\psi}_f$ is the dissipated energy per unit volume which along with macroscopic the strain-stress response can be used to calibrate a bulk damage model [74].

We compare macroscopically homogenized strain versus stress responses in Fig. 18. Unlike Fig. 17, the portion of response past failure is not depicted to concentrate only on elastic to full damage transition. As mentioned, having a larger variation on initial crack length distribution
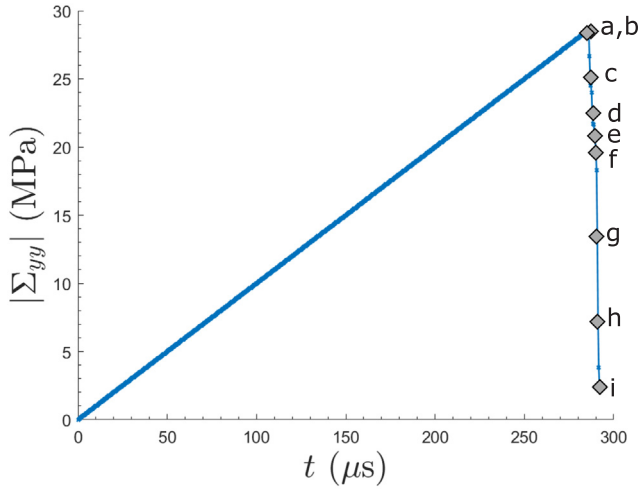
Fig. 25. Macroscopically homogenized stress $|\Sigma_{yy}|$ versus time for the compressive loading example. The detailed solution for different stages of solutions are shown in Fig. 26.

for $m = \frac{1}{2}$ results in higher variations and generally lower values for averaged mesoscale fracture strengths; *cf.* Figs. 9 and 12 ($L_{SVE} = 1$). Having smaller minimum strengths (s_c and $\widetilde{s}$), results in earlier time for failure initiation $\widetilde{t}_i$ (thus smaller $\widetilde{E}_i$ and $\widetilde{\Sigma}_i$) in Figs. 17 and 18. The smaller minimum and overall strength values for s_c also results in a weaker rock compare to other m values, particularly $m = 4$. This is reflected in its much smaller macroscopic tensile strength. Finally, larger standard deviation in microcrack length (and thus mesoscopic strength $\widetilde{s}$), results in an expanded time and strain range for transition from the initiation of nonlinear response to maximum stress stages in Figs. 17 and 18, respectively.

Table 2 compares time, strain, stress, and energy density scales of all Weibull distributions at different stages of macroscopic solution. As discussed above, $m = \frac{1}{2}$ has the lowest nonlinear response initiation time/strain/stress and maximum stress. These trends continue as m increases until the maximum values are realized for $m = 4$. Again, the reason for this trend is the higher minimum and overall mesoscopic fracture strengths $\widetilde{s}$ as m increases. Specifically, we observe that nonlinear response in terms of time, strain, and stress starts 4.28 times earlier for $m = \frac{1}{2}$ compared to $m = 4$. In addition, $m = 4$ corresponds to a much stronger rock given that its macroscopic tensile strength ($\widetilde{\Sigma}_m$) is 3.30 times of that of $m = \frac{1}{2}$. Higher stress levels for initiation (i) and maximum stages (m) are the main contributors for the $m = 4$ specimen having the highest toughness as well; the ratio of dissipated energy density $\widetilde{\psi}_f$ of $m = 4$ to $m = \frac{1}{2}$ solution is 6.22, which is at an even higher value than corresponding ratios for tensile strength and nonlinear initiation stress limit.

Next, we study the effect of m on brittleness. As observed in Figs. 17 and 18, once the rock's nonlinear response initiates, it takes much less time and strain for $m = 4$ sample to reach failure stage compared to samples with lower m values. That is, there is much less time and a smaller deformation safety zone for this rock once failure initiates. This is reflected in a very high *brittleness factor* $\widetilde{t}_i/\widetilde{t}_f = \widetilde{E}_f/\widetilde{E}_i = 0.97$ for $m = 4$ compared to 0.60 for $m = \frac{1}{2}$.

From an energy perspective, $\widetilde{\psi}_i/\widetilde{\psi}_m$ is the ratio of elastic energy stored up to the initiation of nonlinear response to the energy consumed at the onset of unstable unloading. Moreover, $\widetilde{\psi}_m/\widetilde{\psi}_f$ represents the ratio of energy at the onset of unloading to the total dissipated energy at failure. These measures are deemed to represent the energy brittleness indicators for the loading and unloading phases. As can be seen from all proposed measures of brittleness, $m = \frac{1}{2}$ and $m = 4$ samples are the least and most brittle ones. In summary, while a higher m corresponds to a higher strength and tougher rock, the tendency of the mesoscopic

strength $\widetilde{s}$ to a uniform field has the drawback of making the rock more brittle.

4.3. Analysis of crack propagation in the RVE

In this section we study the dynamics of crack propagation and analyze the fracture pattern at different stages of solution. Fig. 19 shows the total length of propagated crack, L, in the domain over time for each Weibull distribution with shape parameter m. As m increases, more time (and therefore, higher stress) is required to initiate crack propagation. This is in agreement with results in Section 4.2. Interestingly, the result for $m = \frac{1}{2}$ does not depict a rapid growth of L. For $m = \frac{1}{2}$ cracks are nucleated (and propagated) at the weakest points in the domain from $\widetilde{t}_i = 46\,\mu s$ to around $t = 65\,\mu s$. However, due to the high variability of mesoscopic strength $\widetilde{s}$, crack tips may be surrounded by much higher strength rock. About $20\,\mu s$ time is needed to build up the overall stress field sufficiently high to enable the propagation of a crack through the surrounding area, explaining the rather slow crack growth rate during this period. In contract, for higher m values mesoscopic strength field is more uniform. Thus, once the first cracks are nucleated there is a faster growth of L.

Another observation is the continued growth of L past the failure stage for all m values. For example, for $m = \frac{1}{2}$, $\widetilde{t}_f = 76\,\mu s$ whereas L growth significantly slows down only at $t \approx 140 - 170\,\mu s$, corresponding to about three full cycles of $\widetilde{\Sigma}_{yy}$ oscillations past $\widetilde{t}_f$ in Fig. 17. This is due to the dynamic nature of the loading; finite speed cracks and microcracks continue to propagate even past macroscopic failure time $\widetilde{t}_f$ until their growth is slowed down at a later time due to ever reducing overall stress level shown in Fig. 17.

To have a better understanding on degradation and energy dissipative role of propagated cracks, beside the total length of cracks we monitor the level of damage parameter D on crack segments. As a crack grows, D evolves over almost all parts of it that are partially debonded. The regions close to the crack tip have the smallest damage value as the damage evolution has just started therein. In contrast, the tails of the larger cracks often experience full damage. The average damage parameter, $\overline{D}$, computed over all crack segments and weighted by their length in the averaging process is a good measure of the overall level of debonding on all crack segments. The time history of $\overline{D}$ is shown in Fig. 20. For $m = \frac{1}{2}$ in the time range of $\widetilde{t}_i = 46\,\mu s$ to around $t = 65\,\mu s$, we observe a relatively high variation to $\overline{D}$ caused mainly by small length of propagated cracks in Fig. 19. However, for all m values once sufficient length of crack is developed, $\overline{D}$ settles in the range [0.75, 0.82]. That $\overline{D}$ does not tend to unity, *i.e.* full damage, for all crack segments is contributed to dynamic nature of loading and microcracking phenomenon (shown in subsequent figures); while major cracks mostly experience full damage, many microcracks emanated from them experience only partial damage as the local damage driving stress magnitudes may subdue faster than the rate at which damage evolves on their surfaces.

The propagation of cracks in the domain are shown in Figs. 21 and 22. In these figures, each extreme of the Weibull shape parameters, $m = \frac{1}{2}$ and 4 are shown. The strain energy density is $U := \frac{1}{2}\sigma : \epsilon$, where σ and ϵ are the stress and strain tensors. The kinetic energy density is $K = \frac{1}{2}\rho\mathbf{v} \cdot \mathbf{v}$, where ρ is the mass density and $\mathbf{v}$ is the velocity vector. In Fig. 21 and all subsequent solution visualization U is mapped to color field, where zero to maximum values are mapped to blue-to-purple color range. The unit of U is J/m³ = Pa. Similarly, K is mapped to the height field such that regions of high kinetic energy density appear closer.

Different stages of the solutions in these figures are marked in the time history of macroscopic stress in Fig. 17. For both m values, maximum stress $\widetilde{\Sigma}_m$ corresponds to early stages of solution, where mainly horizontally propagating cracks have traversed only a part of the domain. Regions of high strain concentration are observed around moving
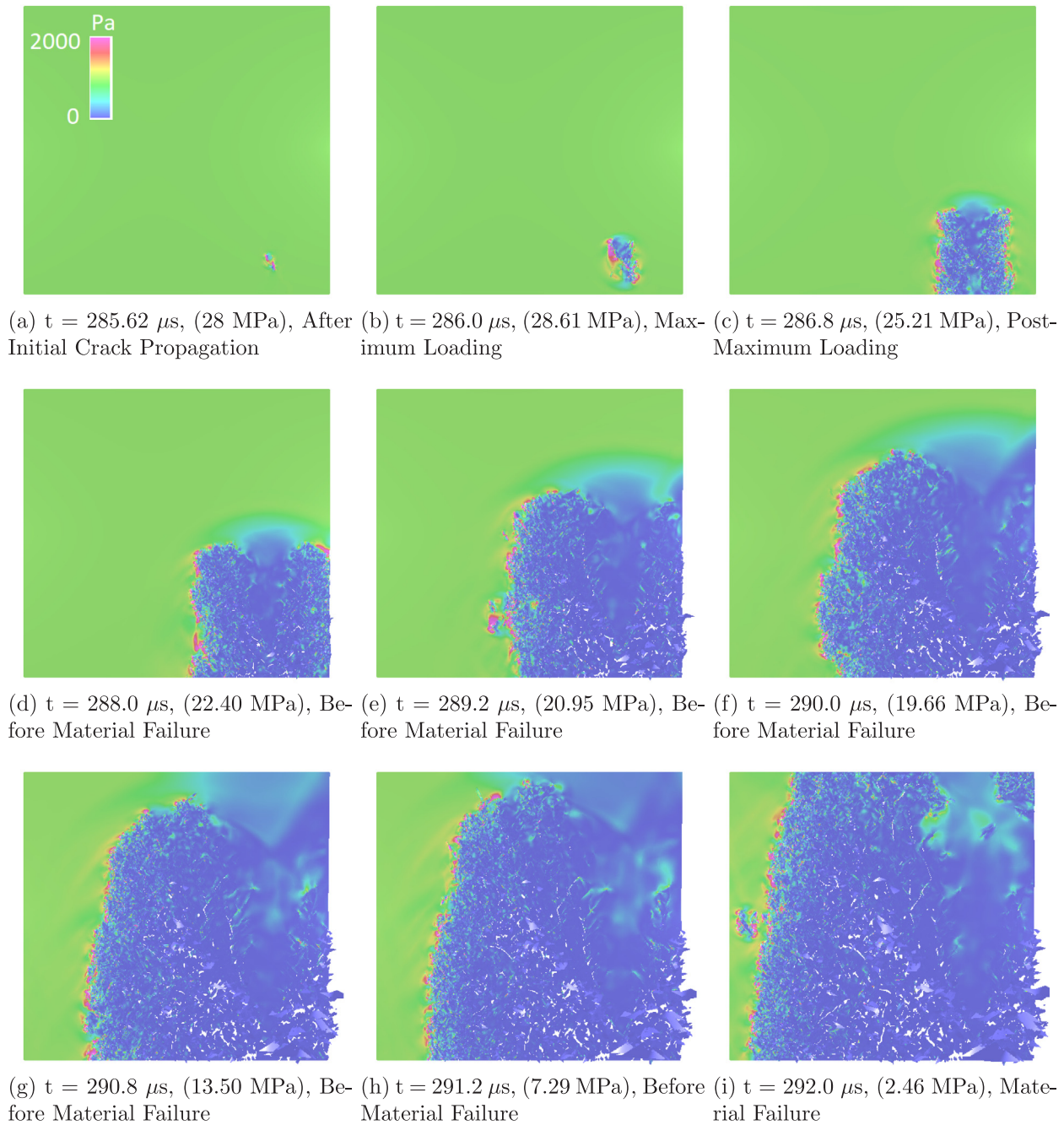
(a) t = 285.62 μs, (28 MPa), After Initial Crack Propagation
(b) t = 286.0 μs, (28.61 MPa), Maximum Loading
(c) t = 286.8 μs, (25.21 MPa), Post-Maximum Loading
(d) t = 288.0 μs, (22.40 MPa), Before Material Failure
(e) t = 289.2 μs, (20.95 MPa), Before Material Failure
(f) t = 290.0 μs, (19.66 MPa), Before Material Failure
(g) t = 290.8 μs, (13.50 MPa), Before Material Failure
(h) t = 291.2 μs, (7.29 MPa), Before Material Failure
(i) t = 292.0 μs, (2.46 MPa), Material Failure

Fig. 26. aSDG solution visualization for the compressive loading example. Color and height fields depict internal and kinetic energy densities, respectively. Numbers in parentheses are $|\Sigma_{yy}|$.

crack tips and on the fronts of propagating elastic waves. Moreover, the stress field relaxes in tail of the cracks as debonding occurs. As shown in Fig. 17, past the failure time $\widetilde{t}_f$ the macroscopic stress Σ_{yy} oscillates about zero and is dampened with each successive oscillation from further failure of rock and dissipation of energy on fracture surfaces. This is also reflected in decreased levels of strain energy densities at latter frames of the solutions shown in Figs. 21 and 22. In comparison of the two sets of solution, fracture initiates later for $m = 4$, involves higher stress values, more abruptly reaches the failure stage, and results in a more widespread and dense network of cracks and microcracks.

Fig. 23 shows the aSDG spatial front meshes for the dynamic fracture simulations at $\widetilde{t}_m$, the time of maximum stress $\widetilde{\Sigma}_{yy}$. As discussed, $\widetilde{t}_m$ increases as m increases. Sections of the crack length which have already failed are indicated by a red line; locations where damage is

occurring (often close to crack tips) are indicated by lines of varying rainbow color from blue to red, corresponding to $D \in [0, \ 1]$. Generally speaking, each crack distribution appears very similar, containing from one to three zones of mostly horizontal and damaged cracks and ranging in size from only about 10% to 20% of the domain width. These cracks are nucleated from locations of low mesoscopic strength $\widetilde{s}$. It is emphasized that all these simulations have started from the relatively coarse spatial mesh (front mesh) shown in Fig. 15b and have resulted in much smaller elements around propagating crack tips; mesh refinement and coarsening operations in spacetime ensure that the differential equations are accurately and efficiently solved on fracture surfaces and in the bulk, and to accommodate arbitrary requested angles of crack propagation.

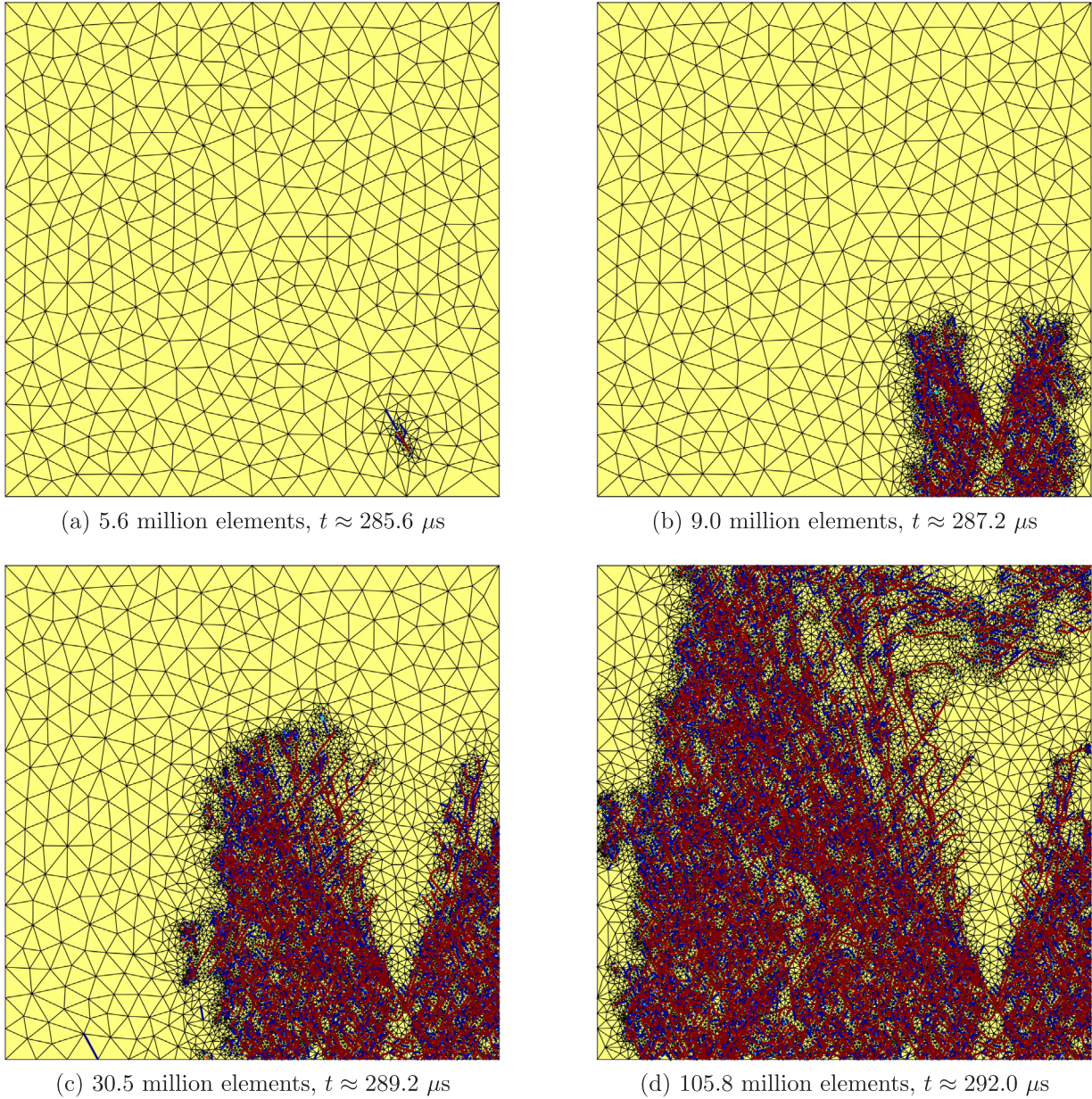Finally, Fig. 24 shows the deformed shape of the domain and crack

(a) 5.6 million elements, $t \approx 285.6 \ \mu s$

(b) 9.0 million elements, $t \approx 287.2 \ \mu s$

(c) 30.5 million elements, $t \approx 289.2 \ \mu s$

(d) 105.8 million elements, $t \approx 292.0 \ \mu s$

Fig. 27. aSDG front meshes for the compressive loading example at different solution times.

pattern at $\widetilde{t}_f$, the time $\widetilde{\Sigma}_{yy}$ crosses zero. At failure for all domains except for $m = 1$, the crack has continued to propagate from the initial damage to completely intersect the domain such that the lower half has been completely separated from the upper domain. As discussed before, the more inhomogeneous mesoscopic fracture strength field for $m = \frac{1}{2}$, resulted in an earlier initiation and slower progression for crack nucleation and growth. We believe that the more gradual nature of crack propagation is the cause of the less complex fracture pattern for $m = \frac{1}{2}$. The higher complexity and density of the fracture network for higher m values is contributed to the more sudden process of failure and more homogeneous mesoscopic fracture strength fields.

4.4. A compressive rock fracture example

While the preceding examples are for a macroscopic tensile loading problem, rock is often under ambient compressive stress condition. Thus, a fracture problem under uniaxial compressive loading is presented for completeness. The problem description is exactly the same as the tensile examples, with the difference that an opposite loading rate is

used in (9); that is, $\dot{\sigma} = -10^{11}$ Pa/s, corresponding to strain rates $a = 0.6/\text{s}$ and $b = -1.4/\text{s}$ in (8).

In rock mechanics Mohr-Coulomb (MC), Hoek-Brown [75], or other *failure criteria* are used for modeling fracture. As detailed in [76,22], some of these models such as MC are not appropriate for tensile fracture. That was the motivation of using MCSC criterion for tensile fracture in preceding sections; *cf.* Section 4.1. We employ an unmodified MC failure criterion for this problem. The form of the corresponding effective stress model in terms of friction angle ϕ and traction components t_n and t_s is provided in [22].

Another challenge in compressive fracture is that crack surfaces are often closed and crack propagates in mode II, that is through frictional sliding of crack surfaces. We have provided dynamic *Riemann solutions* for contact-stick and contact-slip conditions in [58] and incorporated them into an interfacial contact/fracture model for rock in [77]. These Riemann target values are required for implementing such interface conditions in aSDG and other discontinuous Galerkin methods. The details of the model, including transitions and required regularization between contact and separation, and between stick and slip modes are
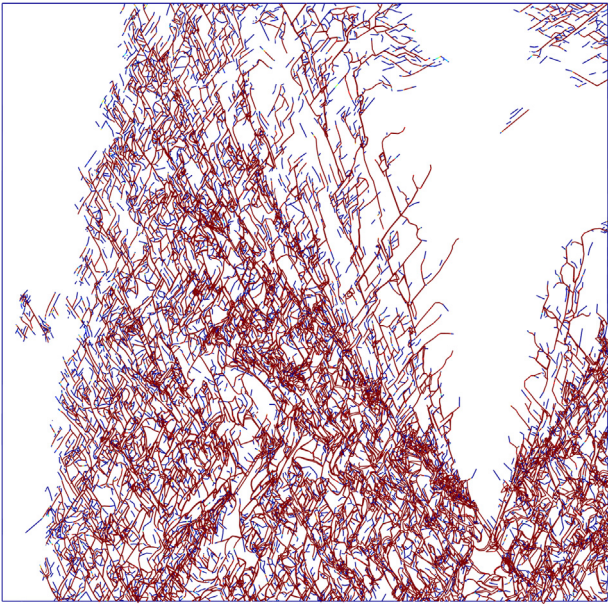
Fig. 28. aSDG deformed shape for the compressive loading example at $t = 292.0$ μs.

provided in [77]. In short, computational modeling of rock fracture under compressive loading is generally more challenging and expensive than under tensile loading. This has in part been the motivation for using a tensile loading scenario for more detailed analyses in Sections 4.2 and 4.3.

Fig. 25 shows macroscopically homogenized stress versus time for a domain where mesoscopic fields are obtained for $L_{SVE} = 1$ and Weibull parameter $m = \frac{1}{2}$. We observe that the maximum compressive stress increases by a factor of 4.75, compared to the corresponding tensile value in Fig. 17 (6 MPa vs. 28.6 MPa). The internal and kinetic energy densities for different stages of solutions are shown in Fig. 26. Similar to tensile loading problems, *cf.* Fig. 23, very little damage and crack propagation is observed at the maximum stress stage.

We note that the tensile or compressive macroscopic stress histories are not compared with experimental results. In [43], S19 sample (whose statistics has been the basis of our synthetic microcrack population at the micro-scale) has been used for a computational compressive example. The *Rock Failure Process Analysis* method (based on the linear finite element method) and quasi-static loading regime are used in [43], whereas herein the aSDG method is used for dynamic simulations under low loading rates. Albeit these and other notable differences in terms of computational domain size and loading, there is a reasonable agreement between the results; in [43] a maximum stress of about 40 MPa is obtained for S19 at the macroscale and similar to Fig. 25, there is a rather sharp softening response past the maximum stress. We believe that the use of experimentally measured parameters of interfacial damage model, such as relaxation time and mode mixity parameter [21], and better representation of the experimental setting (boundary conditions, specimen size, and loading rate) would enhance the accuracy of macroscopic simulations. However, a more detailed calibration of the macroscopic model is beyond the scope of this manuscript.

Fig. 27 shows four different stages of solution in terms of total solved finite elements. Since the front meshes are asynchronous, the minimum time of the entire front mesh is reported for each stage. Similar to tensile examples, advance mesh adaptive operations enable exact tracking of cracks by refining and aligning element boundaries with crack directions. As shown most cracks propagate from the first nucleated crack in the lower right corner of the domain. The final fracture pattern for this problem is shown in Fig. 28. For a uniaxial

compressive loading, the MC criterion predicts the planes with angles $\pm (45° - \phi/2) \approx \pm 29.5°$ with respect to the loading (*i.e.* vertical) direction to satisfy the failure criterion first [22]. In fact, we observe that many cracks are aligned close to this angle. Finally, it is noted that the spatial front in Fig. 27(d) and Fig. 28 contains 80,850 triangles and 41,884 crack segments with a total length of five meters.

5. Conclusion

To incorporate the effect of rock microstructure, we employ a homogenization approach to derive a mesoscopic fracture strength at the center of circular SVEs that traverse a microcracked rock domain. The fracture strength of an SVE is taken as the minimum strength of microcracks contained in or intersecting it; the sliding-wing crack model in [43] is used to compute individual strength of such cracks and take their interaction into account. The homogenization of the effect of microcracks to mesoscale drastically reduces computational cost compared to explicit representation of microcracks and direct numerical simulation of fracture at macroscale. Moreover, by using the microcrack statistics of a real material, Yuen-Long marble from [43], and homogenization by SVEs a direct connection was established between the microscale and the mesoscale fracture strength field.

In [43] microcrack length is assumed to follow a power law distribution. In addition to modeling this distribution, the effect of changing the distribution shape was investigated by using four different shape parameters m for the Weibull distribution; for consistency with the original rock mass, the mean of crack length was kept fixed. Lower values of m result in a larger standard deviation for crack length, which translates to a higher variation and overall lower strengths for the homogenized mesoscopic fracture strength field. We demonstrated that the SVE size has a similar effect, in that by increasing L_{SVE} the mean and standard deviation of mesoscopic strength decrease. This *size effect* was quantitatively analyzed. We also studied the effect of crack density ε_0 on homogenized strength. Due to maintaining a higher level of material inhomogeneity, smaller SVEs are preferred for brittle fracture analysis; however, there is a limit to L_{SVE}. For example, at low crack densities, for small L_{SVE} many SVEs do not contain any cracks and are not representative of the local response.

We use the homogenized mesoscopic fracture strength fields for different Weibull m parameters for a macroscopic uniaxial tensile problem. The SVE size $L_{SVE} = 1$ was chosen as it provides the highest heterogeneity for mesoscopic strength fields without having the problem of being too small for $\varepsilon_0 = 0.243$. Homogenizing the strain and stress tensors at the macroscale revealed that RVE with the highest Weibull parameter $m = 4$ had about 3 times the tensile strength and 6 times the toughness of the RVE with the lowest $m = \frac{1}{2}$. However, the more uniform length distribution of microcracks for higher m values results in a more instantaneous mode of failure, with a more widespread and complex fracture pattern. Therefore, the gains in strength and toughness are offset by a more brittle fracture response. While for all m, the microcracked domains are synthesized and the closest model to the real S19 sample in [43] is for $m = \frac{1}{2}$, this example demonstrates the great impact material microstructure has on its macroscopic response. Thus, accurate characterization and modeling of microstructure is of utmost importance in failure analysis of quasi-brittle materials. Finally, while the macroscopic results, *e.g.*, Figs. 21–24, are not compared with any experimental results, we note that the use of an inhomogeneous fracture strength field is crucial in capturing realistic fracture patterns; otherwise, as shown in [39], the use of a homogeneous strength field can result in nonphysical sudden nucleation of cracks almost everywhere in the domain.

We demonstrate the effectiveness of the SVE homogenization approach for modeling rock fracture. There are; however, several areas of improvement for future research. First, the current process assumes a fully isotropic strength field. For rock with bedding planes, fracture strength should be homogenized as an anisotropic field and calibrated

to appropriate fracture models, *e.g.*, those in [78,79]. Second, we acknowledge that the macroscopic fracture results are not validated against experimental results. For more realistic failure analysis, as in [80] other fields such as elasticity tensor should be considered random and inhomogeneous. Experimental results can be used to calibrate both elastic and fracture properties of inhomogeneous rock [81] and calibrate certain parameters of the interfacial damage model that were missing in the present study. Third, by increasing the number of statistical realizations to more than the one considered herein, a more accurate estimation of the statistical variation of the ultimate macroscopic fracture strength is obtained; see for example [82]. Fourth, in Section 4 we used (6) for modeling microcrack interaction. More realistic interaction models can either be calibrated from experimental results [83] or the analysis of microcrack propagation and interaction in tensile model. Fifth, microcrack-based bulk damage models [84,54,74,85,86] can be much more efficient than the interfacial damage model considered herein and can even be employed in accurate hybrid diffuse damage and interfacial cracking approaches [87]. Moreover, for compressive fracture, microcrack propagation and frictional sliding can be homogenized into bulk damage and plasticity models [88]. The calibration and use of these models is especially important when the simulation of many statistical realizations is needed.

Acknowledgements

References

[1] Rinaldi A, Krajcinovic D, Mastilovic S. Statistical damage mechanics and extreme value theory. Int J Damage Mech 2007;16(1):57–76.

[2] Genet M, Couegnat G, Tomsia A, Ritchie R. Scaling strength distributions in quasi-brittle materials from micro- to macro-scales: a computational approach to modeling nature-inspired structural ceramics. J Mech Phys Solids 2014;68(1):93–106.

[3] Bazant ZP, Le J-L. Probabilistic mechanics of quasibrittle structures: strength, lifetime, and size effect. Cambridge University Press; 2017.

[4] Yin X, Chen W, To A, McVeigh C, Liu W. Statistical volume element method for predicting microstructure-constitutive property relations. Comput Methods Appl Mech Eng 2008;197(43–44):3516–29.

[5] Al-Ostaz A, Jasiuk I. Crack initiation and propagation in materials with randomly distributed holes. Eng Fract Mech 1997;58(5–6):395–420.

[6] Kozicki J, Tejchman J. Effect of aggregate structure on fracture process in concrete using 2D lattice model. Arch Mech 2007;59(4–5):365–84.

[7] Bazant ZP, Planas J. Fracture and size effect in concrete and other quasibrittle materials vol. 16. CRC Press; 1997.

[8] Matouš K, Geers MG, Kouznetsova VG, Gillman A. A review of predictive nonlinear theories for multiscale modeling of heterogeneous materials. J Comput Phys 2017;330:192–220.

[9] Hassold G, Srolovitz D. Brittle fracture in materials with random defects. Phys Rev B (Condens Matter) 1989;39(13):9273–81.

[10] Schlangen E, Garboczi E. Fracture simulations of concrete using lattice models: computational aspects. Eng Fract Mech 1997;57(2–3):319–32.

[11] Doltsinis I, Dattke R. Numerical experiments on the rupture of brittle solids - variation of microstructure, loading and dimensions. Int J Solids Struct 2005;42(2):565–79.

[12] Manzato C, Alava M, Zapperi S. Damage accumulation in quasibrittle fracture. Phys Rev E 2014;90(1):012408.

[13] Silling SA, Askari E. A meshfree method based on the peridynamic model of solid mechanics. Comput Struct 2005;83(17–18):1526–35.

[14] Munjiza A. The combined finite-discrete element method vol. 32. Wiley Online Library; 2004.

[15] Jing L, Stephansson O. Fundamentals of discrete element methods for rock engineering: theory and applications vol. 85. Elsevier; 2007.

[16] Fascetti A, Bolander JE, Nisticó N. Lattice discrete particle modeling of concrete under compressive loading: multiscale experimental approach for parameter determination. J Eng Mech 2018;144(8):04018058.

[17] Clarke PL, Abedi R. Modeling the connectivity and intersection of hydraulically loaded cracks with in-situ fractures in rock. Int J Numer Anal Methods Geomech 2018;42(14):1592–623.

[18] Marteau E, Andrade JE. A model for decoding the life cycle of granular avalanches in a rotating drum. Acta Geotech 2018;13(3):549–55.

[19] Weibull W. A statistical theory of the strength of materials. R Swed Inst Eng Res 1939:Res. 151.

[20] Weibull W. A statistical distribution function of wide applicability. J Appl Mech 1951;18:293–7.

[21] Abedi R, Haber RB, Clarke PL. Effect of random defects on dynamic fracture in quasi-brittle materials. Int J Fract 2017;208(1–2):241–68.

[22] Abedi R, Haber R, Elbanna A. Mixed-mode dynamic crack propagation in rocks with contact-separation mode transitions. Proceeding: 51th US rock mechanics/geomechanics symposium, 2017, ARMA 17-0679. 2017.

[23] Ostoja-Starzewski M. Microstructural randomness versus representative volume element in thermomechanics. J Appl Mech Trans ASME 2002;69(1):25–35.

[24] Matheron G. The theory of regionalized variables and their applications. Paris: Centre de Geostatistique, Fontainebleau; 1971. p. 211.

[25] Cailletaud G, Jeulin D, Rolland P. Size effect on elastic properties of random composites. Eng Comput 1994;11(2):99–110.

[26] Kanit T, Forest S, Galliet I, Mounoury V, Jeulin D. Determination of the size of the representative volume element for random composites: statistical and numerical approach. Int J Solids Struct 2003;40(13):3647–79.

[27] Suquet P. Continuum micromechanics. CISM Courses and Lectures 272.

[28] Liu WK, Siad L, Tian R, Lee S, Lee D, Yin X, et al. Complexity science of multiscale materials via stochastic computations. Int J Numer Meth Eng 2009;80(6–7):932–78.

[29] Ostoja-Starzewski M. Material spatial randomness: from statistical to representative volume element. Probab Eng Mech 2006;21(2):112–32.

[30] Tregger N, Corr D, Graham-Brady L, Shah S. Modeling the effect of mesoscale randomness on concrete fracture. Probab Eng Mech 2006;21(3):217–25.

[31] Baxter S, Graham L. Characterization of random composites using moving-window technique. J Eng Mech 2000;126(4):389–97.

[32] Huyse L, Maes M. Random field modeling of elastic properties using homogenization. J Eng Mech 2001;127(1):27–36.

[33] Segurado J, LLorca J. Computational micromechanics of composites: the effect of particle spatial distribution. Mech Mater 2006;38(8–10):873–83.

[34] Taylor LM, Chen E-P, Kuszmaul JS. Microcrack-induced damage accumulation in brittle rock under dynamic loading. Comput Methods Appl Mech Eng 1986;55(3):301–20.

[35] Homand-Etienne F, Hoxha D, Shao J. A continuum damage constitutive law for brittle rocks. Comput Geotech 1998;22(2):135–51.

[36] Shao J, Rudnicki J. A microcrack-based continuous damage model for brittle geomaterials. Mech Mater 2000;32(10):607–19.

[37] Nguyen VP, Stroeven M, Sluys LJ. Multiscale continuous and discontinuous modeling of heterogeneous materials: a review on recent developments. J Multiscale Model 2011;3(04):229–70.

[38] Lu Y, Elsworth D, Wang L. Microcrack-based coupled damage and flow modeling of fracturing evolution in permeable brittle rocks. Comput Geotech 2013;49:226–44.

[39] Clarke P, Abedi R, Bahmani B, Acton K, Baxter S. Effect of the spatial inhomogeneity of fracture strength on fracture pattern for quasi-brittle materials. Proceedings of ASME 2017 international mechanical engineering congress & exposition IMECE 2017. 2017. p. V009T12A045 (9 pages).

[40] Garrard JM, Abedi R, Clarke PL. Modeling of rock inhomogeneity and anisotropy by explicit and implicit representation of microcracks. Proceeding: 52nd US rock mechanics/geomechanics symposium, 2018, ARMA 18-151-0228-1094. 2018. p. 10.

[41] Garrard JM, Abedi R, Clarke PL. Statistical volume elements for the characterization of angle-dependent fracture strengths. ASME 2018 international mechanical engineering congress and exposition. American Society of Mechanical Engineers; 2018. pp. V009T12A045–V009T12A045.

[42] Wong RH, Chau K, Wang P. Microcracking and grain size effect in yuen long marbles. Int J Rock Mech Min Sci Geomech Abstr 1996;33(5):479–85.

[43] Wong T-F, Wong RH, Chau K, Tang C. Microcrack statistics, Weibull distribution and micromechanical modeling of compressive failure in rock. Mech Mater 2006;38:664–81.

[44] Ashby M, Hallam S. The failure of brittle solids containing small cracks under compressive stress states. Acta Metall 1986;34(3):497–510.

[45] Abedi R, Haber RB, Petracovici B. A spacetime discontinuous Galerkin method for elastodynamics with element-level balance of linear momentum. Comput Methods Appl Mech Eng 2006;195:3247–73.

[46] Abedi R, Haber RB, Thite S, Erickson J. An h–adaptive spacetime–discontinuous Galerkin method for linearized elastodynamics. Revue Européenne de Mécanique Numérique (Eur J Comput Mech) 2006;15(6):619–42.

[47] Acton K, Sherod C, Bahmani B, Abedi R. Effect of volume element geometry on convergence to a representative volume. ASCE-ASME J Risk Uncertainty Eng Syst Part B: Mech Eng 2019;5(3):030907.

[48] Acton K, Graham-Brady L. Meso-scale modeling of plasticity in composites. Comput Methods Appl Mech Eng 2009;198(9):920–32.

[49] Acton K, Graham-Brady L. Fitting an anisotropic yield surface using the generalized method of cells. Advances in mathematical modeling and experimental methods for materials and structures. Springer; 2009. p. 27–41.

[50] Carmeliet J, Hens H. Probabilistic nonlocal damage model for continua with random field properties. J Eng Mech 1994;120(10):2013–27.

[51] Zhou F, Molinari J. Stochastic fracture of ceramics under dynamic tensile loading. Int J Solids Struct 2004;41(22–23):6573–96.

[52] Schicker J, Pfuff M. Statistical modelling of fracture in quasi-brittle materials. Adv Eng Mater 2006;8(5):406–10.

[53] Levy S, Molinari J. Dynamic fragmentation of ceramics, signature of defects and scaling of fragment sizes. J Mech Phys Solids 2010;58(1):12–26.

[54] Daphalapurkar N, Ramesh K, Graham-Brady L, Molinari J. Predicting variability in the dynamic failure strength of brittle materials considering pre-existing flaws. J Mech Phys Solids 2011;59(2):297–319.

[55] Acton KA, Baxter SC, Bahmani B, Clarke PL, Abedi R. Voronoi tessellation based

statistical volume element characterization for use in fracture modeling. Comput Methods Appl Mech Eng 2018;336:135–55.

[56] Dugdale DS. Yielding of steel sheets containing slits. J Mech Phys Solids 1960;8:100–4.

[57] Barenblatt GI. The mathematical theory of equilibrium of cracks in brittle fracture. Adv Appl Mech 1962;7:55–129.

[58] Abedi R, Haber RB. Spacetime simulation of dynamic fracture with crack closure and frictional sliding. Adv Model Simul Eng Sci 2018;5(1):22. Equal contribution authorship.

[59] Abedi R, Hawker MA, Haber RB, Matouš K. An adaptive spacetime discontinuous Galerkin method for cohesive models of elastodynamic fracture. Int J Numer Meth Eng 2009;1:1–42.

[60] Bouchard P-O, Bay F, Chastel Y. Numerical modelling of crack propagation: automatic remeshing and comparison of different criteria. Comput Methods Appl Mech Eng 2003;192(35–36):3887–908.

[61] Paulino GH, Park K, Celes W, Espinha R. Adaptive dynamic cohesive fracture simulation using nodal perturbation and edge-swap operators. Int J Numer Meth Eng 2010;84(11):1303–43.

[62] Park KS, Paulino GH, Celes W, Espinha R. Adaptive mesh refinement and coarsening for cohesive zone modeling of dynamic fracture. Int J Numer Meth Eng 2012;92(1):1–35.

[63] Rangarajan R, Lew AJ. Universal meshes: a method for triangulating planar curved domains immersed in nonconforming meshes. Int J Numer Meth Eng 2014;98(4):236–64.

[64] Belytschko T, Black T. Elastic crack growth in finite elements with minimal remeshing. Int J Numer Methods Eng 1999;45(5):601–20.

[65] Moës N, Dolbow J, Belytschko T. A finite element method for crack growth without remeshing. Int J Numer Meth Eng 1999;46(1):131–50.

[66] Dolbow J, Moës N, Belytschko T. Discontinuous enrichment in finite elements with a partition of unity method. Finite Elem Anal Des 2000;36(3–4):235–60.

[67] Duarte CA, Babuška I, Oden JT. Generalized finite element methods for three-dimensional structural mechanics problems. Comput Struct 2000;77(2):215–32.

[68] Strouboulis T, Babuka I, Copps K. The design and analysis of the generalized finite element method. Comput Methods Appl Mech Eng 2000;181:43–69.

[69] Abedi R, Omidi O, Enayatpour S. A mesh adaptive method for dynamic well stimulation. Comput Geotech 2018;102:12–27.

[70] Zhuang X, Augarde C, Mathisen K. Fracture modeling using meshless methods and level sets in 3d: framework and modeling. Int J Numer Meth Eng 2012;92(11):969–98.

[71] Abedi R, Chung S-H, Erickson J, Fan Y, Garland M, Guoy D, et al. Spacetime meshing with adaptive refinement and coarsening. Proceedings of the twentieth annual symposium on computational geometry, SCG '04. Brooklyn, New York, USA: ACM; 2004. p. 300–9.

[72] Erdogan F, Sih G. On the crack extension in plates under plane loading and transverse shear. J Basic Eng 1963;85(4):519–25.

[73] Nemat-Nasser S, Hori M. Micromechanics: overall properties of heterogeneous materials. Amsterdam; New York: Elsevier; 1993.

[74] Ren X, Chen J-S, Li J, Slawson T, Roth M. Micro-cracks informed damage models for brittle solids. Int J Solids Struct 2011;48(10):1560–71.

[75] Hoek E, Brown ET. Underground excavations in rock. CRC Press; 1980.

[76] Sharpe J, Labuz J, et al. Failure of rock under tensile-compressive loading. 51st US rock mechanics/geomechanics symposium. American Rock Mechanics Association; 2017.

[77] Abedi R, Clarke PL. A computational approach to model dynamic contact and fracture mode transitions in rock. Comput Geotech 2019;109:248–71.

[78] Pietruszczak S, Mroz Z. Formulation of anisotropic failure criteria incorporating a microstructure tensor. Comput Geotech 2000;26(2):105–12.

[79] Pietruszczak S, Lydzba D, Shao J. Modelling of inherent anisotropy in sedimentary rocks. Int J Solids Struct 2002;39(3):637–48.

[80] Hun D-A, Guilleminot J, Yvonnet J, Bornert M. Stochastic multi-scale modeling of crack propagation in random heterogeneous media. Int J Numer Methods Eng 2018.

[81] Pourahmadian F, Guzina BB. On the elastic anatomy of heterogeneous fractures in rock. Int J Rock Mech Min Sci 2018;106:259–68.

[82] Mashhadian M, Abedi S, Noshadravan A. A probabilistic multiscale approach for modeling poromechanical properties of shales. 52nd US rock mechanics/geomechanics symposium. American Rock Mechanics Association; 2018.

[83] Pourahmadian F, Guzina B, et al. Active ultrasonic imaging and interfacial characterization of stationary and evolving fractures in rock. 50th US rock mechanics/geomechanics symposium. American Rock Mechanics Association; 2016.

[84] Graham-Brady L. Statistical characterization of meso-scale uniaxial compressive strength in brittle materials with randomly occurring flaws. Int J Solids Struct 2010;47(18–19):2398–413.

[85] Zhao L, Zhu Q, Xu W, Dai F, Shao J. A unified micro-mechanics-based damage model for instantaneous and time-dependent behaviors of brittle rocks. Int J Rock Mech Min Sci 2016;84:187–96.

[86] Dubey V, Abedi S, Noshadravan A. Multiscale modelling of microcrack-induced mechanical properties in shales. 52nd US rock mechanics/geomechanics symposium. American Rock Mechanics Association; 2018.

[87] Zhao L, Zhu Q, Shao J. Analysis of localized cracking in quasi-brittle materials with a micro-mechanics based friction-damage approach. J Mech Phys Solids 2018;119:163–87.

[88] Zhao L, Zhu Q, Shao J. A micro-mechanics based plastic damage model for quasi-brittle materials under a large range of compressive stress. Int J Plast 2018;100:156–76.